

Transition from spot to faculae domination

An alternate explanation for the dearth of intermediate *Kepler* rotation periods

Timo Reinholt^{1,2}, Keaton J. Bell^{1,2}, James Kuszlewicz^{1,2}, Saskia Hekker^{1,2}, Alexander I. Shapiro¹

¹ Max-Planck-Institut für Sonnensystemforschung, Justus-von-Liebig-Weg 3, 37077 Göttingen, Germany

² Stellar Astrophysics Centre, Department of Physics and Astronomy, Aarhus University, 120 Ny Munkegade, Building 1520, DK-8000 Aarhus C, Denmark

Received day month year / Accepted day month year

ABSTRACT

Context. The study of stellar activity cycles is crucial to understand the underlying dynamo and how it causes magnetic activity signatures such as dark spots and bright faculae. Having knowledge about the dominant source of surface activity might allow us to draw conclusions about the star's age and magnetic field topology, and to put the solar cycle in context.

Aims. We investigate the underlying process that causes magnetic activity by studying the appearance of activity signatures in contemporaneous photometric and chromospheric time series.

Methods. Lomb-Scargle periodograms are used to search for cycle periods present in the photometric and chromospheric time series. To emphasize the signature of the activity cycle we account for rotation-induced scatter in both data sets by fitting a quasi-periodic Gaussian process model to each observing season. After subtracting the rotational variability, cycle amplitudes and the phase difference between the two time series are obtained by fitting both time series simultaneously using the same cycle period.

Results. We find cycle periods in 27 of the 30 stars in our sample. The phase difference between the two time series reveals that the variability in fast rotating active stars is usually in anti-phase, while the variability of slowly rotating inactive stars is in phase. The photometric cycle amplitudes are on average six times larger for the active stars. The phase and amplitude information demonstrates that active stars are dominated by dark spots, whereas less active stars are dominated by bright faculae. We find the transition from spot to faculae domination at the Vaughan-Preston gap, and around a Rossby number equal to one.

Conclusions. We conclude that faculae are the dominant ingredient of stellar activity cycles at ages $\gtrsim 2.55$ Gyr. The data further suggest that the Vaughan-Preston gap can not explain the previously detected dearth of *Kepler* rotation periods between 15–25 days. Nevertheless, our results led us to propose an explanation for the rotation period dearth to be due to the non-detection of periodicity caused by the cancellation of dark spots and bright faculae at ~ 800 Myr.

Key words. stars: activity – stars: rotation – stars: individual: HD 1835, HD 10476, HD 13421, HD 18256, HD 20630, HD 25998, HD 35296, HD 39587, HD 72905, HD 75332, HD 81809, HD 82443, HD 82885, HD 103095, HD 115383, HD 115404, HD 120136, HD 124570, HD 129333, HD 131156A, HD 143761, HD 149661, HD 158614, HD 161239, HD 182572, HD 185144, HD 190007, HD 201091, HD 201092, HD 206860

1. Introduction

In the mid Sixties, O.C. Wilson and collaborators started flux measurements at the centers of the Ca II H+K lines “[...] for the purpose of initiating a search for stellar analogues of the solar cycle.” (Wilson 1968). Ten years later, Wilson (1978) presented long-term Ca II H+K flux measurements of 91 main-sequence stars, providing the first evidence for cyclic activity in some stars. Over the years an empirical activity index describing the emission in the H and K line cores was established (Vaughan et al. 1978), now referred to as the Mount Wilson S-index. This index can be converted into the chromospheric H and K line surface flux (Middelkoop 1982; Rutten 1984). Subtracting the photospheric flux from this quantity, one arrives at the currently most commonly used activity indicator $\log R'_{HK}$, where R'_{HK} denotes the chromospheric flux in the Ca II H+K lines normalized by the bolometric flux (Linsky et al. 1979; Noyes et al. 1984).

Most stellar activity cycles known these days rely on periodicities measured in long-term observations of the S-index (Baliunas et al. 1995; Saar & Brandenburg 1999; Böhm-Vitense

2007). Constraining the basic physical parameters that determine the nature of the activity cycle, especially its period, is a matter of current research. Various authors (Saar & Brandenburg 1999; Böhm-Vitense 2007; Lehtinen et al. 2016) identified a strong dependence of the cycle period on the rotation period, and, as a consequence thereof, the existence of certain sequences (*active* and *inactive* sequence) in the $P_{\text{rot}} - P_{\text{cyc}}$ plane. Böhm-Vitense (2007) suggested that the two distinct sequences might indicate the existence of two dynamos operating at different depths in the star. In contrast, the work by Reinholt et al. (2017) and Saikia et al. (2018) strongly question the existence of the two sequences, especially for the *active* sequence. Moreover, Metcalfe et al. (2016) and Metcalfe & van Saders (2017) proposed a secular increase of the cycle period once the star reaches a critical Rossby number $\text{Ro} \sim 2$.

The periodic changes of the Ca II H+K emission originate from a change in the magnetic field generated by the stellar dynamo. Concurrently, the emergence of active regions in the photosphere (such as dark spots and bright faculae) is expected during activity maximum, as is observed in the Sun. Over the course of the solar cycle, variability is seen both in the total solar irra-

Send offprint requests to: T. Reinholt, e-mail: reinhold@mps.mpg.de

diance (TSI) data (e.g. Shapiro et al. 2016), as well as in the S-index (e.g. Egeland et al. 2017). In the Sun the photometric (TSI) and chromospheric time series (disk-integrated Ca II K-line) are in phase (Preminger et al. 2011). At activity maximum the Sun is brightest due to the presence of bright faculae regions, slightly overcompensating the contributions of dark spots.

Active stars are known to show photometric variability caused by dark spots and bright faculae, as well as enhanced chromospheric emission in the Ca II H+K line cores. Whether all active stars exhibit an underlying activity cycle, i.e., if the surface activity changes periodically or randomly over time, is hitherto hardly known. We aim to understand the physical mechanism that drives long-term photometric and chromospheric brightness variations. To reach this goal, we search for cycle periods in contemporaneous photometric and chromospheric time series. Assuming a common origin of the periodicity, we fit the same cycle period to both time series, which allows us to measure photometric and chromospheric amplitudes, and the phase difference between the variations in both time series. We show that the phase difference reveals the dominant type of stellar activity, i.e., dark spots or bright faculae. Moreover, the phase difference shows a strong dependence on the stellar activity level, the rotation period, and the photometric amplitude. These correlations may help to understand stellar dynamos as a function of activity level, rotation period, and age. In the following we study a sample of 30 stars, for which chromospheric activity cycles have been reported for 18 stars (17 in Baliunas et al. 1995, 14 in Saikia et al. 2018, and 6 in Olspt et al. 2017), and photometric activity cycles for 6 stars (Messina & Guinan 2002). Taking advantage of analyzing both time series simultaneously, we detect activity cycles in 27 stars in total. In 8 stars thereof, activity cycles have not been measured before.

2. Data

In the current study, data from three different sources have been used. Long-term V band and Strömgren b and y photometric time series have successfully been requested from Messina & Guinan (2002) and Lockwood et al. (2007), respectively. For all stars, chromospheric emission data from the Mount Wilson survey are publicly available¹. In total our sample contains 30 stars. The Julian date range, number of data points, mean time stamp, brightness, and standard deviation of each observing season is listed in appendices A and B for the photometric and chromospheric time series, respectively. Their basic stellar parameters are listed in Table 1. Effective temperatures, surface gravities and metallicities are taken from the references given. The spectral types have been adopted from Messina & Guinan (2002) and Lockwood et al. (2007). The different data sets are briefly described in the following.

2.1. Photometric data

Messina & Guinan (2002, 2003) studied the long-term magnetic activity of five young solar analogues (HD 1835, HD 20630, HD 72905, HD 129333, HD 206860), and a young K dwarf (HD 82443). These authors compiled photometric observations available from the literature (with different band passes) and new observations taken in Johnson V band into one time series covering up to \sim 16 years. The authors state that the typical stan-

dard deviation of the V band magnitudes is equal to 0.007 mag, which we adopt as photometric uncertainty of the measurements. For all stars in their sample, Messina & Guinan (2002, 2003) detected a photometric activity cycle. For details, we refer the reader to the above publications.

Lockwood et al. (2007) presented up to 20 years of differential Strömgren b and y photometry of 32 stars with contemporaneous observations of the Mount Wilson S-index (see also Lockwood et al. 1997; Radick et al. 1998, 2018) with the purpose of studying long-term photometric and chromospheric variability. We received data for 26 out of the 32 stars in their sample. Photometric uncertainties σ_{by} have been adopted from Table 2 in Lockwood et al. (2007). In total, our sample consists of 30 stars as two stars (HD 1835 and HD 129333) are present in both photometric samples.

2.2. Chromospheric emission data

The Mount Wilson survey has taken chromospheric emission data from 1966-1995 for the majority of stars in their sample, and for 35 stars until the year 2001. Thereof, 24 stars belong to our sample and have been observed for more than 33 years. The remaining six stars have shorter observing time spans between 9 to 28 years. Recently, this unprecedented data set became publicly available¹. The Mount Wilson S-index is the main quantity of interest describing the amount of chromospheric emission in the centers of the Ca II H+K lines. A definition of this quantity can be found in Vaughan et al. (1978). From the year 1977 on, an observational weight, WT , accounting for the photon noise is supplied. This weight can be converted into a relative S-index uncertainty $\sigma_S/S = WT^{-1/2}$ (Duncan et al. 1991). These uncertainties were used in our computations whenever available.

3. Detection of activity cycle period and phase

In Fig. 1 we show an example of contemporaneous photometric (top panel) and chromospheric (bottom panel) observations. Both time series show short-term (seasonal) variability, partly caused by active regions on the stellar surface rotating in and out of view, and long-term brightness changes over several seasons, possibly caused by an underlying activity cycle. However, detecting a cycle period (and in a next step, the phase difference between the two time series) is challenging because the scatter in the individual observing seasons hampers the detection of long-term brightness changes. In the following we present a model capable of detecting stellar rotation signals. This model is applied to each observing season and subtracted from the data in order to enhance the visibility of the signal from the activity cycle. Afterwards we search for a cycle period present in both time series in order to compute the phase difference between the two time series.

3.1. The Gaussian process model

To account for the variation due to stellar rotation in each observing season, we apply a quasi-periodic Gaussian process² (GP) model that accounts for periodic and long-term trends in the data. The GP was implemented using the python package George (Ambikasaran et al. 2015). A quasi-periodic GP model has successfully been applied to *Kepler* data to infer stellar rotation periods (Angus et al. 2018). The underlying kernel function

¹ The data can be found at ftp://solis.nso.edu/MountWilson_HK/ and a brief manual at ftp://solis.nso.edu/MountWilson_HK/HK_data_ReadMe.docx.

² An introduction to Gaussian process regression can be found in Rasmussen & Williams (2005).

HD	Name	Object type	SpT	T_{eff} (K)	$\log g$ (dex)	Fe/H (dex)	Reference
1835	9 Cet	BY*	G2.5 V	5723 $^{+148}_{-41}$	4.48 $^{+0.14}_{-0.09}$	0.19 $^{+0.04}_{-0.01}$	Boeche & Grebel (2016)
10476	107 Psc	PM*	K1 V	5125 $^{+30}_{-49}$	4.47 $^{+0.03}_{-0.04}$	-0.04 $^{+0.04}_{-0.04}$	Boeche & Grebel (2016)
13421	64 Cet	PM*	G0 IV	6066 $^{+30}_{-42}$	3.81 $^{+0.09}_{-0.09}$	0.14 $^{+0.04}_{-0.04}$	Niedzielski et al. (2016)
18256	ρ Ari	SB*	F6 V	6380 $^{+80}_{-80}$	4.17 $^{+0.20}_{-0.20}$	-0.23 $^{+0.10}_{-0.10}$	Balachandran (1990)
20630	κ^1 Cet	BY*	G5 V	5605 $^{+55}_{-15}$	4.40 $^{+0.07}_{-0.02}$	0.04 $^{+0.03}_{-0.01}$	Boeche & Grebel (2016)
25998	50 Per	RS*	F7 V	6147 $^{+70}_{-70}$	4.35 $^{+0.10}_{-0.10}$	-0.11 $^{+0.10}_{-0.10}$	Chen et al. (2000)
35296	111 Tau	BY*	F8 V	6171 $^{+63}_{-63}$	4.31 $^{+0.09}_{-0.09}$	0.01 $^{+0.05}_{-0.05}$	Prugniel et al. (2011)
39587	χ^1 Ori	RS*	G0-V	5935 $^{+89}_{-16}$	4.52 $^{+0.06}_{-0.06}$	0.00 $^{+0.04}_{-0.01}$	Boeche & Grebel (2016)
72905	π^1 UMa	BY*	G1.5 V	5814 $^{+67}_{-19}$	4.55 $^{+0.08}_{-0.09}$	-0.06 $^{+0.03}_{-0.01}$	Boeche & Grebel (2016)
75332	-	PM*	F7 Vn	6130 $^{+70}_{-70}$	4.32 $^{+0.10}_{-0.10}$	0.00 $^{+0.10}_{-0.10}$	Chen et al. (2000)
81809	-	SB*	G2 V	5667 $^{+18}_{-102}$	3.85 $^{+0.03}_{-0.14}$	-0.37 $^{+0.02}_{-0.03}$	Boeche & Grebel (2016)
82443	DX Leo	BY*	K0 V	5334 $^{+80}_{-80}$	4.40 $^{+0.17}_{-0.17}$	-0.03 $^{+0.08}_{-0.08}$	Mishenina et al. (2013)
82885	11 LMi	RS*	G8 IV-V	5438 $^{+47}_{-58}$	4.34 $^{+0.14}_{-0.03}$	0.33 $^{+0.02}_{-0.02}$	Boeche & Grebel (2016)
103095	-	PM*	G8 V	4947 $^{+75}_{-80}$	4.56 $^{+0.07}_{-0.28}$	-1.41 $^{+0.04}_{-0.03}$	Boeche & Grebel (2016)
115383	η Vir	PM*	G0 Vs	6087 $^{+100}_{-12}$	4.42 $^{+0.08}_{-0.02}$	0.13 $^{+0.03}_{-0.01}$	Boeche & Grebel (2016)
115404	-	**	K1 V	4901 $^{+47}_{-25}$	4.43 $^{+0.07}_{-0.02}$	-0.17 $^{+0.01}_{-0.02}$	Boeche & Grebel (2016)
120136	τ Boo	**	F6 IV	6462 $^{+78}_{-16}$	4.37 $^{+0.13}_{-0.02}$	0.15 $^{+0.03}_{-0.01}$	Boeche & Grebel (2016)
124570	14 Boo	**	F6 IV	6109 $^{+100}_{-100}$	3.85 $^{+0.10}_{-0.10}$	0.07 $^{+0.10}_{-0.10}$	Takeda (2007)
129333	EK Dra	BY*	G0 V	5700 $^{+70}_{-70}$	4.37 $^{+0.10}_{-0.10}$	-0.16 $^{+0.07}_{-0.07}$	König et al. (2005)
131156A	ξ Boo A	PM*	G8 V	5410 $^{+0}_{-0}$	4.48 $^{+0.00}_{-0.00}$	-0.05 $^{+0.00}_{-0.00}$	Boeche & Grebel (2016)
143761	ρ CrB	PM*	G0+ Va	5745 $^{+14}_{-89}$	3.99 $^{+0.06}_{-0.09}$	-0.30 $^{+0.02}_{-0.02}$	Boeche & Grebel (2016)
149661	12 Oph	BY*	K2 V	5156 $^{+30}_{-14}$	4.47 $^{+0.03}_{-0.05}$	0.05 $^{+0.01}_{-0.01}$	Boeche & Grebel (2016)
158614	-	SB*	G9 IV-V	5461 $^{+35}_{-24}$	4.20 $^{+0.08}_{-0.02}$	-0.02 $^{+0.02}_{-0.01}$	Boeche & Grebel (2016)
161239	84 Her	PM*	G2 IIIb	5742 $^{+15}_{-15}$	3.68 $^{+0.04}_{-0.04}$	0.21 $^{+0.02}_{-0.02}$	Niedzielski et al. (2016)
182572	31 Aql	PM*	G7 IV	5561 $^{+60}_{-43}$	4.12 $^{+0.14}_{-0.02}$	0.34 $^{+0.03}_{-0.02}$	Boeche & Grebel (2016)
185144	σ Dra	PM*	K0 V	5132 $^{+53}_{-28}$	4.35 $^{+0.08}_{-0.03}$	-0.26 $^{+0.02}_{-0.01}$	Boeche & Grebel (2016)
190007	-	BY*	K4 V	4541 $^{+80}_{-43}$	4.26 $^{+0.24}_{-0.02}$	0.11 $^{+0.02}_{-0.05}$	Boeche & Grebel (2016)
201091	61 Cyg A	BY*	K5 V	4310 $^{+61}_{-7}$	4.14 $^{+0.16}_{-0.00}$	-0.36 $^{+0.01}_{-0.02}$	Boeche & Grebel (2016)
201092	61 Cyg B	Fl*	K7 V	3945 $^{+107}_{-9}$	4.03 $^{+0.23}_{-0.10}$	-0.63 $^{+0.07}_{-0.09}$	Boeche & Grebel (2016)
206860	HN Peg	BY*	G0 V	5961 $^{+85}_{-85}$	4.45 $^{+0.03}_{-0.03}$	-0.06 $^{+0.07}_{-0.07}$	Ramírez et al. (2013)

Table 1. Basic stellar parameters of the sample taken from Simbad. Spectral types have been adopted from Messina & Guinan (2002) and Lockwood et al. (2007). The object type reads as follows: BY* = Variable of BY Dra type, RS* = Variable of RS CVn type, PM* = High proper-motion star, SB* = Spectroscopic binary, ** = Double or multiple star, Fl* = Flare star.

of this GP model reads

$$k(x_i, x_j) = \underbrace{h^2 \exp\left(-\frac{(x_i - x_j)^2}{2l^2}\right)}_{\text{SE}} \cdot \underbrace{\exp\left(-\Gamma \sin^2\left[\frac{\pi}{P}(x_i - x_j)\right]\right)}_{\text{ESS}} + \sigma^2 \delta_{ij}. \quad (1)$$

In general, a kernel function $k(x_i, x_j)$ describes the covariance between arbitrary data points x_i and x_j . The quasi-periodic kernel is composed of two well-established kernels, namely the squared exponential (SE) and the exponential sine squared (ESS) kernel. The SE kernel contains the length scale parameter l , which accounts for the covariance between observations taken at times x_i and x_j . The ESS kernel contains two parameters: the period P to account for periodicities in the data, and the parameter Γ to control the harmonic behavior of the periodicity. The parameter h is sometimes called the “amplitude” of the covariance because it is linked to the variance in the time series. The second term, $\sigma^2 \delta_{ij}$, accounts for the white noise in the time series, with δ_{ij} being the Kronecker delta. For all stars in our sample, the rotation periods have been measured (Baliunas et al. 1996), and we use them as initial period guesses P in the GP prediction. Finally the full set of so-called hyper-parameters $\{\sigma, h, l, \Gamma, P\}$ is estimated by fitting the above model to the data assuming Gaussian-distributed uncertainties.

We applied uniform priors to all parameters, with the period being limited to $\pm 30\%$ of the initial value. It is worth noting

that these limits do not exclude possible harmonics of this period needed to fit a double-dip shape in the time series arising from spots on opposite sides of the star. The parameter Γ in the GP accounts for the harmonic behavior of the fit, given an initial period. Additionally, we checked the initial values reported by Baliunas et al. (1996) and Messina & Guinan (2002), and can confirm all rotation periods within $\pm 20\%$.

The parameter estimation is performed using the affine-invariant ensemble sampler emcee (Foreman-Mackey et al. 2013; Goodman & Weare 2010). In total we used 32 walkers and 2000 iterations when running emcee. The walkers were initialized around the solution found by a previous Maximum Likelihood Estimation (MLE) step and in almost all cases this provided a starting point very close to the final parameters found after the MCMC. For each run we calculated the integrated auto-correlation time and thinned the chains accordingly. In addition to computing the effective sample size, we also visually inspected the chains and the marginal posterior distributions to ensure that they looked reasonable. This allows us to estimate the marginalized posterior probability density of the period given the other hyper-parameters. Additionally, the mean flux value of each observing season is predicted by the MCMC sampler.

In Fig. 2 we present data from the observing season indicated by the red box in Fig. 1 and the optimized GP model including 1σ uncertainties. The GP model predicts a rotation period of $P_{\text{rot}} = 7.80$ d, close to the literature value of $P_{\text{rot}} = 7.756$ d

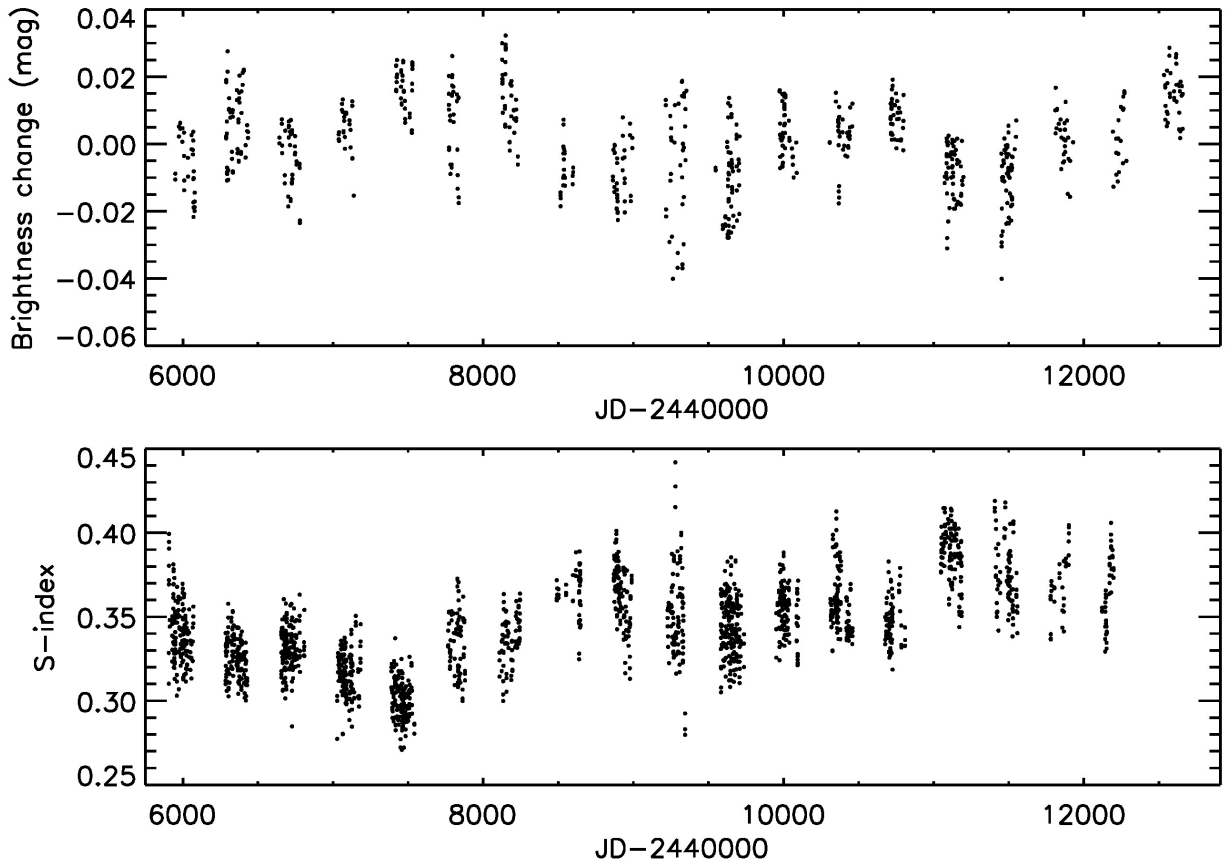


Fig. 1. Photometric (top panel) and chromospheric (bottom panel) time series of the star HD 1835. The red box indicates the observing season shown in Fig. 2.

(Messina & Guinan 2002). The length scale parameter l accounts for long-term trends over the course of the observing season, likely caused by the active regions' lifetimes.

The main purpose of using the GP model is to remove the rotational short-term activity rather than measuring the rotation period (a Lomb-Scargle periodogram or a Fourier transform would be sufficient for the latter). Whenever it was not possible to detect a periodic signal (either due to the absence of active regions or their short life time compared to the stellar rotation period), the GP model predicts a flat line being a fair model in quiet epochs. The GP model presented in Eq. 1 is applied to each observing season in each data set.

3.2. The reduced time series

To remove the rotation signature from each observing season, we subtract the GP model from the data and add the mean flux value of the season as predicted by the MCMC sampler. This preserves the seasonally-averaged mean flux values and pronounces the signature of the activity cycle. The reduced time series of the star HD 1835 is shown in Fig. 3. Comparing the reduced time series to the original data in Fig. 1 shows that the scatter in each season is reduced significantly. Alternatively to using all data points, the time series can be simplified by compressing each season to the predicted mean value, and using the standard deviation of the residuals (i.e. data minus GP model) as uncertainties. Since these uncertainties reflect the residual activity of each season, and not the uncertainty of the predicted mean value, we decided to use

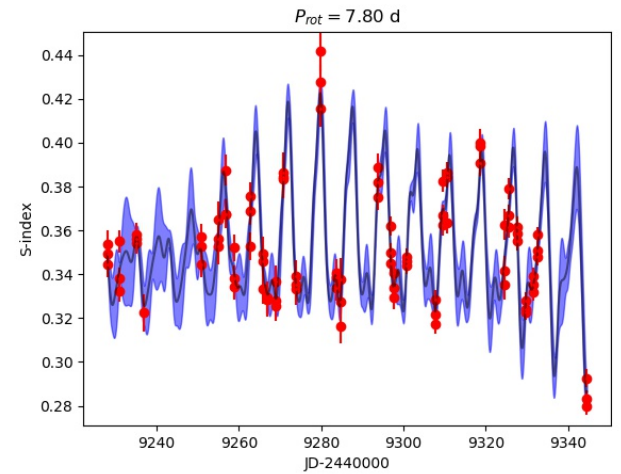


Fig. 2. Selected observing season of Mount Wilson S-index time series of the star HD 1835 (indicated by the red box in Fig. 1). The GP prediction is shown as solid line with the 1σ uncertainties of the prediction in blue. The GP model predicts a rotation period of $P_{\text{rot}} = 7.80$ d.

the full time series in the following. Note that we also searched for cyclic behavior of the rotation periods inferred from the GP analysis as done by Messina & Guinan (2003). These authors interpreted (cyclic) changes of the rotation period in terms of a

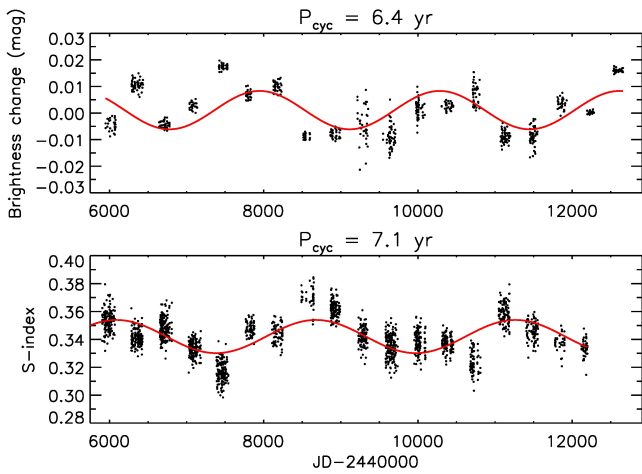


Fig. 3. Reduced photometric (top panel) and chromospheric (bottom panel) time series of Fig. 1. Sine fits to the data are shown in red with their cycle periods given at the top of each panel. In the lower panel a sine wave with a long period of 28.1 yr has been subtracted (see Table 2).

possible butterfly diagram. However, our analysis of the “rotation period time series” does not show a significant cycle period.

The reduced time series are used to search for cycle periods in the following way. Using Lomb-Scargle periodograms (Zechmeister & Kürster 2009) we first search for periodicity in the photometric and chromospheric time series individually. In a second step we search for a single cycle period fitting both data sets at the same time (see Sect. 3.3). However, finding the correct cycle period requires visual inspection of each time series. The data often show long trends on the order of the observing time span, appearing as the highest peak in the periodogram. Whenever periods longer than 75% of the observing time span are detected, we subtract a long sine wave from the data and compute the periodogram again. Since it cannot be decided whether such a trend is caused by a very long activity cycle or if it is an instrumental artifact, we report these long periods in Table 2 as potential long activity cycles.

Another problem arises for the Mount Wilson data before the year 1980. At these early epochs the data sampling is much sparser due to a different observing strategy. It seems that including these early observations generates a long trend over the full observing time span, although no systematic offset or a common trend could be identified for all stars. Thus, for 18 stars in our sample, early Mount Wilson data have been discarded in the further analysis. All Mount Wilson observing seasons used in the following can be found in appendix B.

3.3. Detection of a single cycle period and phase difference

After the subtraction of potential long activity cycles we search for periods present in both the photometric and chromospheric time series. Computing the Lomb-Scargle periodogram and selecting the highest peak usually yields a good estimate of the true cycle period. In Fig. 3 the Lomb-Scargle periodogram returns a cycle period of $P_{\text{cyc}} = 6.4 \text{ yr}$ for the photometric time series, and a cycle period of $P_{\text{cyc}} = 7.1 \text{ yr}$ for the chromospheric time series. To compute the phase difference between the two time series one has to fit the same period in both data sets simultaneously. Thus, a sine fit was applied to fit both time series at

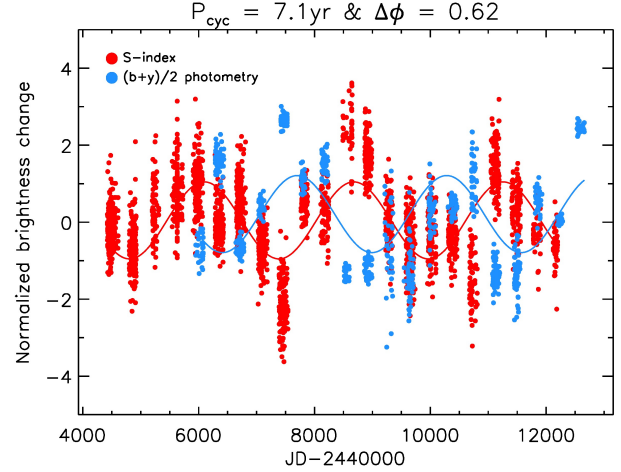


Fig. 4. Photometric (blue) and chromospheric (red) time series of the star HD 1835. The simultaneous sine fit to the data (same colors, respectively) yields a cycle period of $P_{\text{cyc}} = 7.07 \pm 0.02 \text{ yr}$. Both data sets were normalized by their respective sine amplitudes.

the same time using a single period, with individual amplitudes, phases and offsets for the two data sets. As an initial guess of the true cycle period, we use the mean of the cycle periods inferred from the individual time series. The result of the fit to both data sets of HD 1835 simultaneously is shown in Fig. 4. To combine the two different types of data into a dimensionless quantity the time series have been normalized by their sine amplitudes. The simultaneous sine fit returns a single cycle period of $P_{\text{cyc}} = 7.07 \pm 0.02 \text{ yr}$. From this fit we can compute the phase difference between the two time series to check for possible phase shifts. These results are presented in Sect. 4.2. The sine fit was performed using the Levenberg-Marquardt least-squares minimization method. We also tried fitting the sine wave using an MCMC approach to retrieve more realistic uncertainties. This approach did not converge unless we restricted the priors of the parameters to a very small region around the best values returned by the least-squares fit. Given the nature of the model, where interpretability in terms of phase differences is preferred over being optimal in terms of model structure (i.e., more activity cycle-based), the application of MCMC was not ideal and a simpler least-squares approach was favored. Thus, we report the formal uncertainties of the fit parameters, which should be considered as lower limits. We did also try modeling the cycle behavior with the same GP model that was used for the rotation, and use cross correlation to determine the relative phases; however, this was found to be unreliable. A reason that we did not try to add a phase difference into the kernel of the GP is that understanding the behavior of the resulting covariance matrix is not straight forward.

4. Results

4.1. Cycle periods

Cycle periods could be detected for 27 stars in total. These periods are given in Table 2. Following the cycle classification as introduced by Baliunas et al. (1995), we provide a quality flag for each cycle period that has been assigned by visual inspection of both the photometric and the chromospheric time series individually. A higher number indicates stronger periodicity of the data, with integer values between 1 (weak periodicity), and

3 (excellent periodicity). Two example light curves are shown in appendix C. We identified a subset of eight stars exhibiting an excellent chromospheric activity cycle. We return to these stars in Sect. 4.2 and Sect. 5. To quantify the goodness of the periodicity we computed the reduced chi-square values of the fit to each data set individually (χ^2_{phot} and χ^2_{chrom}), and also to both data sets simultaneously (χ^2_{sim}). The values are reported in the last three columns of Table 2. However, we found that these values do not correlate with the periodicity of the data. This is owing to the fact that both the period and the amplitude of the activity cycle can vary from cycle to cycle. For instance, the varying cycle amplitude of the star HD 201091 in the Mount Wilson time series creates quite a high value for χ^2_{chrom} , although the periodicity is evident in this star ($\text{flag}_{\text{chrom}} = 3$). Moreover, the shape of the activity cycle does not need to be sinusoidal (as assumed by the sine fit), even when the period and amplitude are constant over time.

We compare our cycle periods to measurements from the literature in Fig. 5. Panel (a) shows the measurements by Baliunas et al. (1995), that contain all the 30 stars from our sample. These authors found periodicity in 17 out of the 30 stars. We also detect periodicity in these 17 stars, although no periodicity could be detected in the photometric time series of the star HD 201092. In panel (a)-(c) this star is shown as open circle to indicate that the periodicity has only been measured in the chromospheric time series. Taking advantage of up to ten years of additional Mount Wilson data, we detect periodicity in 11 stars where Baliunas et al. (1995) did not report a cycle. Comparing the period measurements to one another generally shows good agreement within $\pm 20\%$ (dotted lines), although some outliers are apparent. In HD 120136, Baliunas et al. (1995) detected a “poor” cycle of ~ 12 yr, which can be disproved by considering the additional data. In HD 149661, these authors detected a “good” cycle of ~ 17.4 yr. Again we cannot confirm this long period, which might be owed to the sparse data of the early observations. For the star HD 190007, Baliunas et al. (1995) detected a “fair” ~ 13.7 yr cycle. This period might be a modulation of the potentially very long cycle of ~ 38 yr that has been subtracted in our analysis. The two stars HD 1835 and HD 115404 lie close to the upper 20% limit. The periods determined by Baliunas et al. (1995) are likely affected by trends in the early observations.

At first glance, the measurements by Saikia et al. (2018) in panel (b) of the 14 stars that we have in common seem to show stronger deviations to our results. The overall bigger deviations might arise from the fact that these authors also considered the much sparser data of the early seasons in their analysis. For HD 1835, HD 82443, and HD 115383, long periods have been subtracted in our analysis, which explains the large deviation. HD 20630 shows a long trend in the early data, which is not visible anymore in the later seasons. Our cycle periods for HD 1835 and HD 20630 have been identified as secondary cycles in Saikia et al. (2018). For HD 149661, Saikia et al. (2018) claimed a primary cycle of 15.3 yr and a secondary cycle of 7.7 yr, respectively. Our analysis does not confirm any of these periods, not even when considering all available “raw” data. Furthermore, we cannot reproduce the period claimed for HD 18256, although the deviation to our results is smaller in this case. For HD 190007, Saikia et al. (2018) claimed a cycle period of 5.4 yr. This period is visible in the computed periodograms with a smaller peak height. Thus, we expect this period to be a modulation of the longer one. Although most deviations can be explained by a different data analysis, some period detections remain mysterious.

A comparison of our results to those by Olspt et al. (2017) in panel (c) shows remarkably good agreement. In total, 17 stars are contained in both samples. All six stars for which both authors detected periodicity almost lie on the 1:1 line. As mentioned above, for the star HD 201092 we do not detect a photometric cycle period. All cycle period detections in panel (a)-(c) are based solely on the Mount Wilson data set. In contrast to Baliunas et al. (1995) and Saikia et al. (2018), Olspt et al. (2017) use a similar approach as described here based on GP models. Additionally, these authors account for long-timescale trends in the time series, which explains the overall good agreement to our results.

Finally, we compare our measurements to the cycle periods detected by Messina & Guinan (2002) in panel (d). In contrast to the measurements in panel (a)-(c), these periods are solely based on photometric data. We find good agreement to our results for five of the six stars within the $\pm 20\%$ range. For HD 72905, two different photometric data sets have been combined in the year 1993 (compare Table 5 and Fig. 6 in Messina & Guinan 2002). Comparing the photometric and the chromospheric time series of this star raises the question whether this combination may have introduced an offset between the different photometric data sets because no such offset is seen in the chromospheric time series. We calculated the median brightness of the data before and after the year 1993, and added the difference to the data taken after the year 1993. This removes the long period found by Messina & Guinan (2002), and yields a cycle period of ~ 4.2 yr, which almost equals twice the period reported by these authors.

4.2. Activity cycle phase difference

The phase difference $\Delta\phi$ between the fits to the photometric and chromospheric time series reveals the dominant source of activity on the stellar surface, e.g., dark spots or bright faculae regions. A phase difference of $\Delta\phi \approx 0$ indicates that the star is brightest at activity maximum. This is the case in the Sun. The opposite case of minimum brightness during activity maximum, i.e. $\Delta\phi \approx 0.5$, demonstrates that the star is dominated by dark spots. In Fig. 6 we show the phase difference $\Delta\phi$ against the mean stellar magnetic activity level $\log R'_{\text{HK}}$.

The maximum phase difference between two time series equals $|\Delta\phi| = 0.5$. In Fig. 6 we plot $\Delta\phi$ between -0.25 and 0.75 to allow for a scatter around $\Delta\phi = 0$ and $\Delta\phi = 0.5$. We find two distinct groups of stars: one scattering around $\Delta\phi = 0.5$ and the other scattering around $\Delta\phi = 0$. The two groups are clearly separated by their mean activity level $\log R'_{\text{HK}}$. The transition from $\Delta\phi = 0.5$ to $\Delta\phi = 0$ occurs around $\log R'_{\text{HK}} \approx -4.75$, the location of the Vaughan-Preston gap (Vaughan & Preston 1980; Noyes et al. 1984, hereafter VP gap). This clear separation tells us that active stars (above the VP gap) are spot-dominated whereas inactive stars (below the VP gap) are faculae-dominated.

As stars age they spin down because angular momentum is lost due to stellar winds. This spin-down is accompanied by a decrease of the magnetic activity (Skumanich 1972). Hence, we expect all stars to transition from spot-dominated to faculae-dominated surface activity, depending on their activity level and age. Taking advantage of the close connection between activity and rotation (Fig. 8 in Noyes et al. 1984), we show the phase difference versus the Rossby number (instead of the activity level on the abscissa) in Fig. 7. The Rossby number $\text{Ro} = P_{\text{rot}}/\tau$ equals the rotation period divided by the convective turnover time τ . The latter has been computed following Noyes et al. (1984). As in Fig. 6, the separation into a spot-dominated and a faculae-dominated group is evident with the active stars at

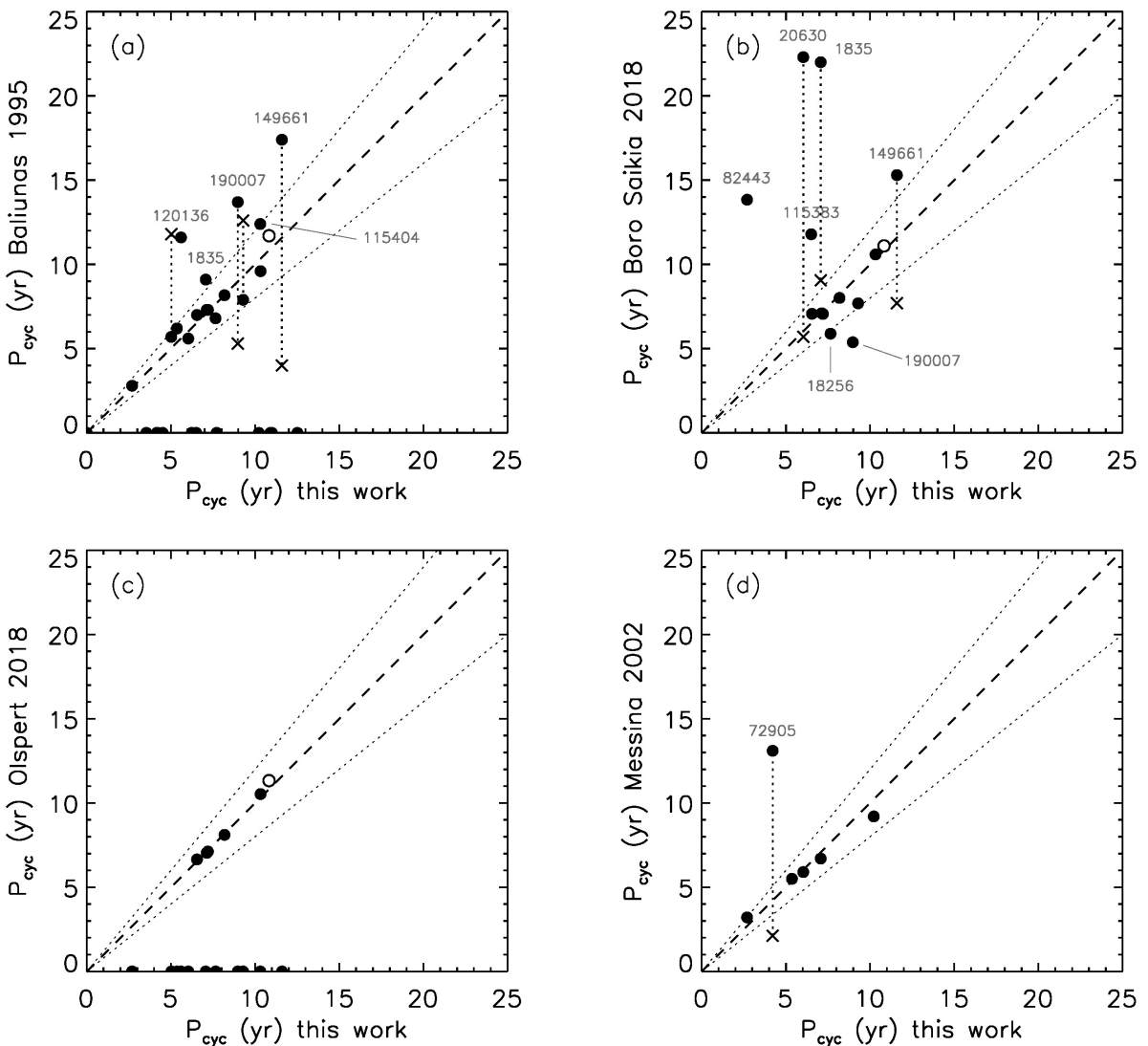


Fig. 5. Comparison of our cycle period measurements to results from (a) Baliunas et al. (1995), (b) Saikia et al. (2018), (c) Olspert et al. (2017), and (d) Messina & Guinan (2002). The open circle indicates the star HD 201092 for which only a chromospheric cycle period was measured. Crosses indicate secondary periods connected by vertical dotted lines to the primary periods. The dashed line shows the 1:1 identity, and the dotted lines to either side mark the $\pm 20\%$ range. We set the cycle period to zero for stars in common for which no cycle period was reported.

$\text{Ro} \lesssim 1$, and the inactive stars at $\text{Ro} \gtrsim 1$. Below $\text{Ro} = 1$ rotation is the driving source for surface activity; above $\text{Ro} = 1$ stars rotate slower, and convection plays a more important role. The advantage of the Rossby number over the rotation periods is that the convective turnover time accounts for the mass dependence of the rotation period.

The presence of two distinct groups in Fig. 8 provides further evidence for our interpretation that stars around $\Delta\phi = 0$ are faculae-dominated and stars around $\Delta\phi = 0.5$ are spot-dominated. The group of spot-dominated stars has on average six-times-larger photometric amplitudes than the faculae-dominated group. This result is consistent with the work of Shapiro et al. (2014), who showed that with the increase of magnetic activity the spot contribution to the photometric variability increases faster than the faculae contribution. Consequently, less active stars with smaller photometric variability are faculae-dominated, while more active stars with larger photometric variability are spot-dominated. The total photometric amplitude of 0.37 mmag for the solar cycle has been computed by Shapiro

et al. (2016). Such a small value was explained in Witzke et al. (2018) by the incident combination of solar fundamental parameters and the spectral location of the Strömgren b and y pass bands. Furthermore, in Table 2 eight of the 27 stars with measured cycle periods exhibit a chromospheric activity cycle classified as excellent (flag_{chrom} = 3). Concurrently, their photometric amplitudes are shallow. All these stars belong to the group around $\Delta\phi = 0$, i.e., they are faculae-dominated.

5. Discussion

Taking advantage of contemporaneous photometric and chromospheric time series, we have determined activity cycle periods and the corresponding phase differences for 27 stars in our sample. For two stars in our sample, no activity cycle could be detected. HD 124570 and HD 143761 both are very inactive and show almost flat variability both in the photometric and the chromospheric time series. HD 201092 shows an activity cycle of

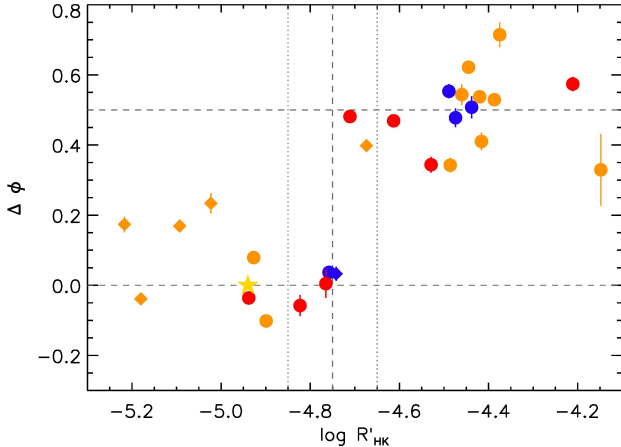


Fig. 6. Activity cycle phase difference $\Delta\phi$ against the magnetic activity index $\log R'_{\text{HK}}$. Dots show dwarf stars (luminosity class V) and diamonds show (sub-)giants (luminosity class III, IV, IV-V). The colors show different spectral types: F stars (blue), G stars (orange), and K stars (red). The vertical dashed line indicates the approximate location of the Vaughan-Preston gap, with its boundaries indicated by the dotted lines, adopted from Fig. 2 of Noyes et al. (1984). The horizontal dashed lines at $\Delta\phi = 0.5$ and $\Delta\phi = 0$ mark the region of spot and faculae domination, respectively. The yellow star indicates the position of the Sun, adopting the mean value $\log R'_{\text{HK}, \text{Sun}} = -4.94$ from Egeland et al. (2017).

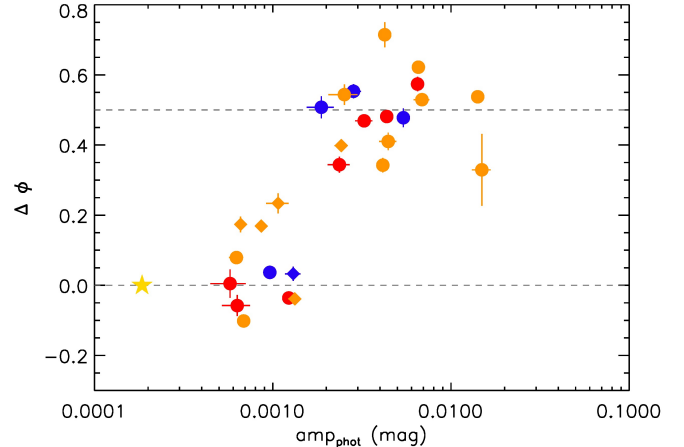


Fig. 8. Activity cycle phase difference $\Delta\phi$ against the photometric sine amplitude. Colors and symbols have the same meaning as in Fig. 6. The photometric amplitude of the solar cycle (yellow star) was adopted from Shapiro et al. (2016). These authors calculated a total amplitude of 0.37 mmag, which results in a sine amplitude of $\text{amp}_{\text{phot}, \text{Sun}} = 0.185$ mmag.

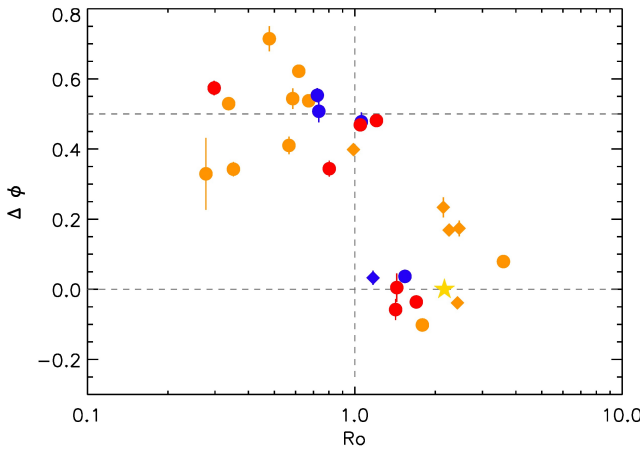


Fig. 7. Activity cycle phase difference $\Delta\phi$ against the Rossby number $\text{Ro} = P_{\text{rot}}/\tau$. Colors, symbols, and horizontal dashed lines have the same meaning as in Fig. 6. The vertical dashed line indicates the transition around $\text{Ro} = 1$. The yellow star indicates the position of the Sun, $\text{Ro}_{\text{Sun}} = 2.16$, adopting the values $B - V_{\text{Sun}} = 0.653$ (Ramírez et al. 2012), and the synodic rotation period $P_{\text{rot}, \text{Sun}} = 26.3$ d.

~10.8 yr in the chromospheric time series, whereas no periodicity could be detected in the photometric time series.

In Figs. 6–8 we showed that faculae-dominated stars are inactive slow rotators with small photometric amplitudes, compared to their active spot-dominated counterparts with shorter rotation periods and larger amplitudes. The transition from spot- to faculae-dominated activity occurs at an activity level of $\log R'_{\text{HK}} \approx -4.75$ (the VP gap), and around a Rossby number $\text{Ro} \approx 1$. This result is consistent with the work of Montet et al. (2017). These authors searched for photometric activity cycles by analyzing *Kepler* full-frame images (FFIs). They corre-

lated the long-term brightness variations of the FFIs with photometric short-term variability measured by the magnetic activity proxy S_{ph} from the *Kepler* light curves (see Mathur et al. 2014). These authors found that most stars with rotation periods shorter than 15–25 days show short-term photometric variability amplitudes that are anti-correlated with the seasonal brightness in the FFIs. This supports the interpretation that the activity cycles of fast rotating stars are spot-dominated. For stars with longer rotation periods, a correlation between short-term variability amplitudes and average brightness suggests that their activity cycles are faculae-dominated. In their sample of Sun-like stars with $0.6 \lesssim B - V \lesssim 0.7$, the rotation period range between 15–25 days marks the transition from spot- to faculae-dominated activity. Using activity-rotation relations from Mamajek & Hillenbrand (2008), this period range coincides with the VP gap, where we find the transition from spot- to faculae-dominated activity. Using the same relations, this period range can be transferred to Rossby numbers: $\text{Ro}(P_{\text{rot}} = 15 \text{ d}) = 1.25$ and $\text{Ro}(P_{\text{rot}} = 25 \text{ d}) = 2.09$ using the mean color $B - V_{\text{mean}} = 0.65$.

To further support the finding of a transition from spot- to faculae-dominated activity, we attempted a similar analysis to Montet et al. (2017) by correlating the following photometric time series: the first one consists of the seasonal mean brightness values, and the second one contains the variability range R_{var} of each observing season (see Basri et al. 2010, 2011). This quantity measures the rotation-induced variability in each season similar to the quantity S_{ph} used by Montet et al. (2017). We correlated these two time series to see whether the long- and short-term variability is in or out of phase. Our results are, however, inconclusive given the relative imprecision of the ground-based data.

Moreover, we find that the majority of faculae-dominated stars in our sample exhibits a chromospheric activity cycle with a strong sinusoidal shape ($\text{flag}_{\text{chrom}} = 3$). All eight of these $\text{flag}_{\text{chrom}} = 3$ stars lie below the VP gap. Activity-age relations from Mamajek & Hillenbrand (2008) reveal ages greater than 2.7 Gyr for these eight stars, suggesting that the transition from complex to sinusoidal or smooth cycles is complete at this age. This confirms earlier results by Oláh et al. (2016) who analyzed

activity cycles of Mount Wilson stars, finding that slowly rotating stars show smooth activity cycles, whereas more rapidly rotating stars exhibit more complex cycles, with a clear transition from complex to smooth cycles at ages between $\sim 2\text{--}3$ Gyr.

For six stars in our sample, the magnetic field topology has been measured from Zeeman Doppler imaging (See et al. 2016). Their results suggest that spot-dominated stars show toroidal fields, whereas faculae-dominated stars exhibit mostly poloidal fields. A toroidal field has indeed been detected in HD 20630 and HD 131156A, for which we detect spot-dominance. HD 10476 and HD 201091 are faculae-dominated stars with smooth chromospheric activity cycle (flag_{chrom} = 3) showing strong poloidal fields and almost no toroidal fields. The spot-dominated star HD 206860 does not fall in either group, showing 50% of each field component, and HD 120136 shows a slightly more toroidal than poloidal field, although our results suggest faculae-dominance for this star. Unfortunately, the number of stars with observed magnetic field topology in overlap with our sample is too small to either confirm or reject the scenario suggested by See et al. (2016).

5.1. Can the VP gap explain the dearth of intermediate rotation periods?

McQuillan et al. (2013) first discovered a dearth of rotation periods around ~ 25 days in the rotation period distribution of the *Kepler* M dwarfs. It has been shown that this dearth extends to hotter stars covering a rotation period range of $\sim 15\text{--}25$ days (Reinhold et al. 2013; McQuillan et al. 2014; Reinhold & Gizon 2015). McQuillan et al. (2013) explained the detected bimodality of the rotation periods by an overlap of two stellar populations of different age in the *Kepler* field, with the younger stars rotating faster, on average, than the older stars. Davenport (2017) also discussed the bimodality seen in the *Kepler* rotation period distribution. By using absolute G-band magnitudes from the Gaia mission, this author demonstrated that the McQuillan et al. (2014) sample might be strongly contaminated by subgiants. Because of their deeper convective envelopes, their rotation period distribution is significantly different from dwarf stars, which might explain the previous non-detection of the bimodality in these stars. Removing those evolved stars from the sample, Davenport (2017) showed that the bimodality persists for stars hotter than 5000 K. This author further finds that the fast and slow rotators in his sample also exhibit a different distribution of the total proper motion. Hence, the existence of two kinematically separate groups would favor the explanation of two epochs of stars formation in the *Kepler* field. This explanation is further supported by the work of Davenport & Covey (2018), showing that the bimodality also correlates with Galactic height, which is assumed to be related to stellar age.

Over the last years it has been discussed whether the lack of intermediate active stars at the VP gap can explain the dearth at intermediate rotation periods. To test this hypothesis, we revisit the rotation period distribution of the *Kepler* sample measured by Reinhold & Gizon (2015) in Fig. 9. The rotation periods are plotted against $B - V$ color, and the data points are color-coded with the variability range R_{var} (we return to this quantity in Sect. 5.2). The dearth of rotation periods becomes visible at ~ 15 days at $B - V \approx 0.9$ and increases to ~ 25 days at $B - V \approx 1.5$. We find that the *Kepler* rotation periods are well represented by gyrochronology relations from Barnes (2010): the blue and red lines show the gyrochronology isochrones (gyrochrones) for ages of 300 Myr and 2550 Myr, respectively. The

color-dependent dearth of rotation periods follows a gyrochronone with an age of ~ 800 Myr (dotted black line).

The age of 2550 Myr has been selected because it refers to the activity level of $\log R'_{\text{HK}} \approx -4.75$ at the VP gap. In Fig. 9 we over-plot the spot- and faculae-dominated stars of the current sample as black and yellow symbols, respectively. For colors $B - V > 0.5$, where gyrochronology relations are well calibrated (Barnes 2007), we find all spot-dominated stars below the 2550 Myr isochrone, and all the faculae-dominated stars above this age. In the color range $B - V < 0.5$ where gyrochronology is not well calibrated we use the same activity-age relations as before to infer the ages of the two F stars HD 18256 and HD 120136. This analysis yields ages of 2.65 Gyr and 2.45 Gyr, respectively, consistent with the age of 2.55 Gyr associated with the activity level at the VP gap. Hence, the expected age of stars at the VP gap clearly separates the spot- and faculae-dominated stars in our sample. This result demonstrates that the observed dearth of stars at an age of ~ 800 Myr can not be explained in terms of the VP gap.

5.2. Alternate explanation for the dearth region

The *Kepler* stars in Fig. 9 are color-coded by their variability range R_{var} , which describes the amplitude of the rotational variability. Interestingly, the dearth region around ~ 800 Myr is dominated by stars with small variability amplitudes (mostly blue points). Moreover, there seems to be a variability gradient towards the dearth region from either side, i.e., stars younger and older than ~ 800 Myr show larger variability. Based on the result that faculae are the dominant ingredient of the surface activity for the activity cycle after 2.55 Gyr, we expect that the faculae surface coverage may increase from an earlier age. To explain both the dearth of stars and the decreased variability, we propose the idea of a period determination bias, and suggest the following scenario: Fast rotating stars are able to generate strong magnetic fields, which in turn create large and long-lived spots. As the stars slow down, the magnetic field topology changes such that the magnetic field is not able to maintain large spots anymore, and instead generates smaller active regions surrounded by bright faculae. This process diminishes the variability amplitudes and continues until faculae become so prominent on the surface that bright and dark active regions partially cancel each other. The stars in the dearth region might have smaller and more homogeneously distributed spots, which simultaneously would decrease the variability, and render period determination more difficult. Hence, many stars with small variability amplitudes will not be detected due to certain amplitude constraints.

To better illustrate the idea of spot and faculae cancellation, we applied the Spectral And Total Irradiance REconstruction (SATIRE, see Fligge et al. 2000; Krivova et al. 2003), which is the state-of-the-art model of solar brightness variations, for synthesizing light curves brought about by the mixture of facular and spot features. Such a model light curve is shown in Fig. 10. We have considered a star with rotational period of 30 days at various inclination angles. The light curve was synthesized for 1400 days, which is comparable to the total duration of the *Kepler* observations. The mean surface coverage of spots was chosen to be 0.1% (i.e. the star is a bit more active than the Sun). We used a log-normal distribution of spot sizes from Baumann & Solanki (2005), and assumed a linear decay of spot sizes with time (following Martinez Pillet et al. 1993). We assumed that each spot is surrounded by a facular region, which is a reasonable assumption for modeling rotational stellar variability (see, e.g. Shapiro et al. 2017). The faculae-to-spot coverage ratio at

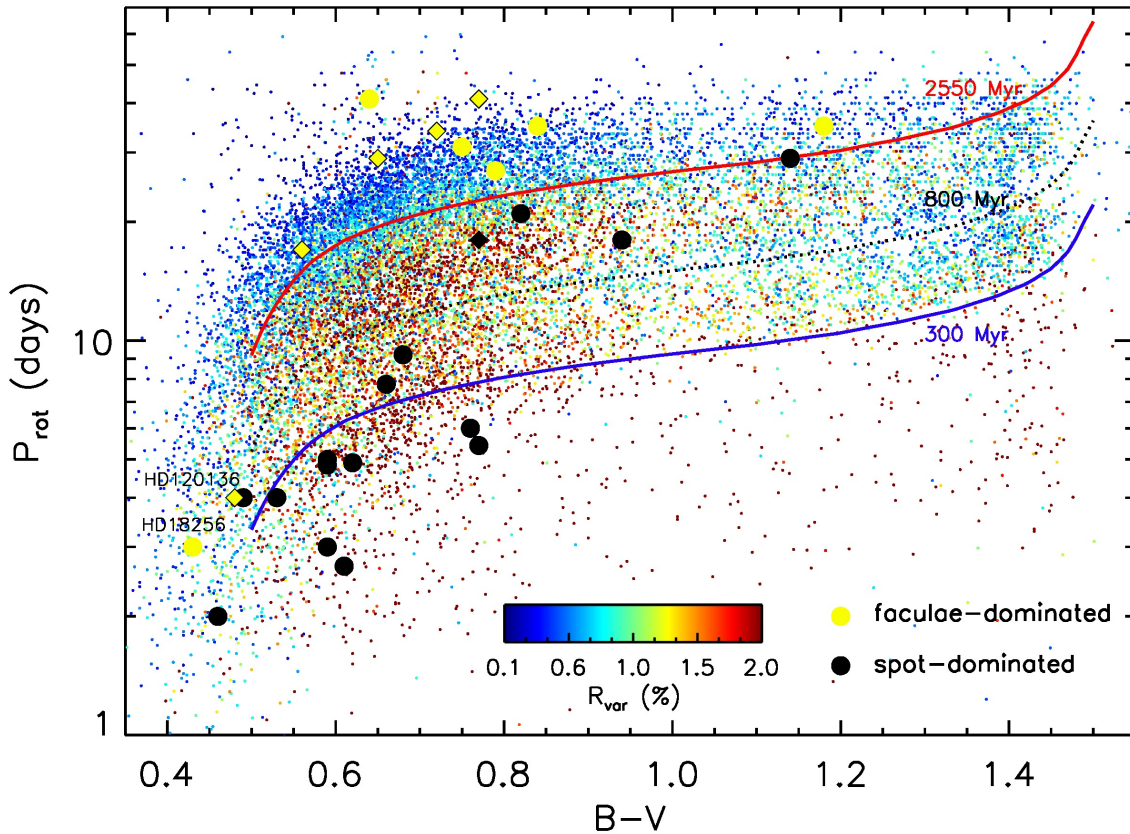


Fig. 9. *Kepler* rotation periods P_{rot} against $B - V$ color taken from Reinhold & Gizon (2015). The data points are color-coded with the variability range R_{var} . Black and yellow symbols show spot- and faculae-dominated stars, respectively, for the current sample. As before dots show dwarf stars (luminosity class V) and diamond show (sub-)giants (luminosity class III, IV, IV-V). The solid blue, dotted black, and solid red lines show 300 Myr, 800 Myr, and 2550 Myr isochrones, respectively, using gyrochronology relations from Barnes (2010).

the day of emergence was taken to be 3.4, and the lifetimes of faculae were considered to be three times longer than those of spots, which roughly corresponds to the solar case.

The lower left panel in Fig. 10 shows the Lomb-Scargle periodogram of the time series. The power was normalized to unity (i.e. perfect sinusoidal periodicity); none of the peaks is significant, following the threshold of a peak height of 0.1 as used by Reinhold & Gizon (2015). The lower right panel shows the auto-correlation function (ACF) of the time series, which was used by McQuillan et al. (2014) to search for periodicity in the *Kepler* sample. The peaks indicate a periodicity with multiples of 10 days, although with low power. The correct rotation period cannot be recovered either by the periodogram or by the ACF method. Thus, we conclude that 1) this star would have been considered as non-periodic using the periodogram approach, or 2) would have been considered as periodic using the ACF method, however measuring a wrong rotation period. This model light curve has a variability range of $R_{\text{var}} = 0.56\%$; if a significant period were detected, it would appear as blue dot in Fig. 9. We note that a similar spot and faculae cancellation happens in the solar case. Shapiro et al. (2017) showed that the 27-day peaks in the spot and facular component of the solar brightness variability (calculated for the period 1996–2015) cancel each other, so that the power spectrum of solar brightness variations is almost flat around the rotational period.

Fig. 9 further shows that the variability increases after an age of ~ 800 Myr, suggesting that spots again become the dominant source of activity. This scenario is supported by the presence of the four spot-dominated stars between the ~ 800 Myr and the 2.55 Gyr isochrone. It is worth mentioning that Lockwood et al. (2007) also detected spot dominance for these four stars. Once the stars slow down further and pass the VP gap, faculae become the dominant source of surface activity on activity cycle time scales. This is supported by the large abundance of stars with small variability amplitudes above the transitional age of 2.55 Gyr. Although the transition from spot to faculae domination has been inferred from variability on activity cycle time scales, this observation suggests that at least some rotation periods have been inferred from long-lived faculae rather than short-lived spots, as seen in the quiet Sun. Based on observations of solar activity this idea has already been proposed by Pettersen et al. (1992). During solar activity maximum bright and dark features cancel each other, hampering a reliable period detection, whereas rotation can be inferred from faculae during activity minimum. To decide on the dominant surface feature spot-crossings during transits (e.g. Morris et al. 2018) or Doppler images would be needed.

We emphasize that classifying a star to be spot- or faculae-dominated refers to the type of feature that causes it to appear overall fainter or brighter during the peaks of its activity cycle. On rotational time scales spots usually are the dominant source

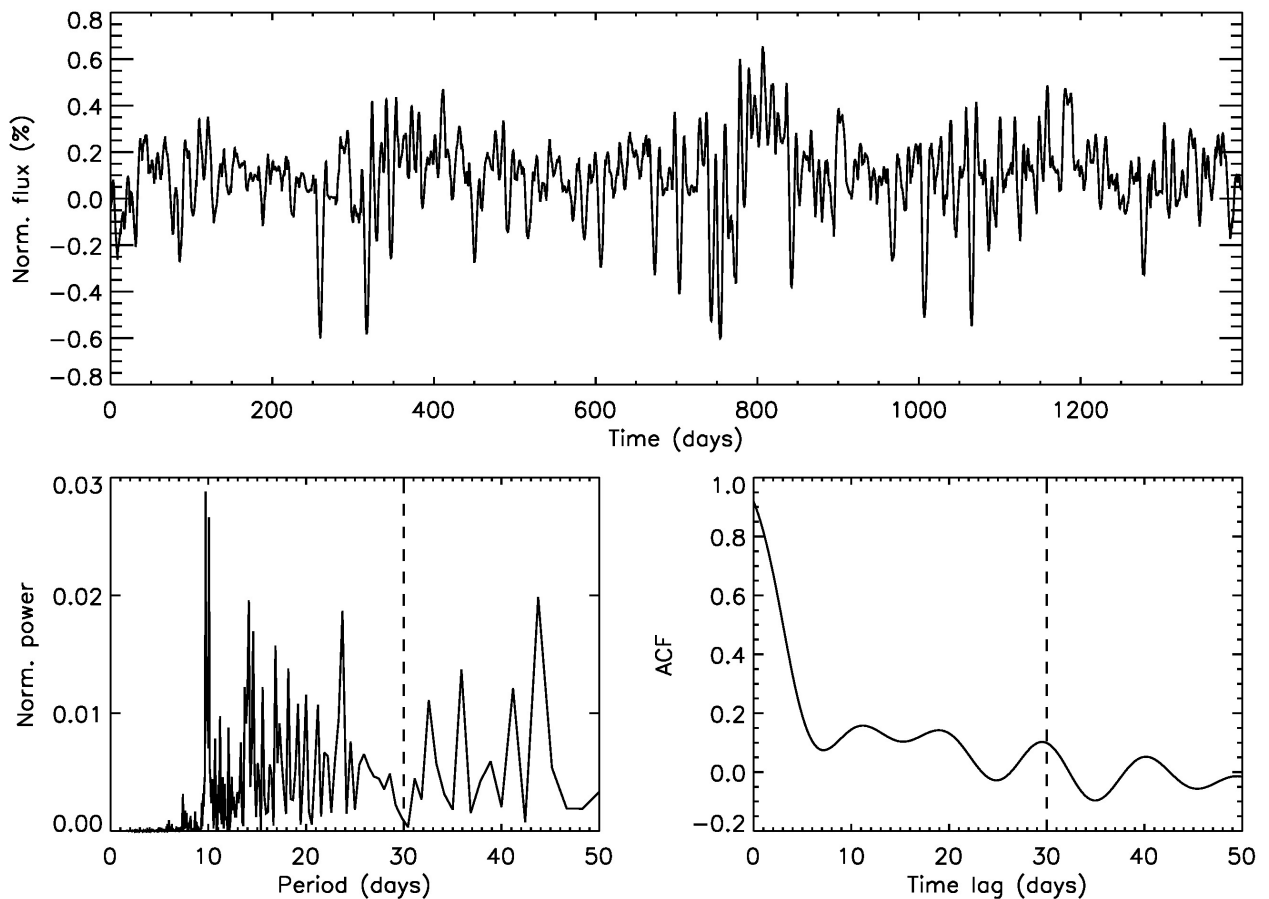


Fig. 10. Top panel: Model light curve with a rotation period of 30 days viewed at an inclination angle of 90 degrees. Lower left: Lomb-Scargle periodogram of the time series. Lower right: auto-correlation function of the time series. The vertical dashed line indicates the model rotation period.

of variability seen in the light curve because they are more localized than faculae (Shapiro et al. 2016). Moreover, faculae-dominated stars older than 2.55 Gyr are still able to maintain spots, as is observed in the Sun. Applying the simultaneous sine fit to the individual observing seasons, and searching for the same rotation period instead of the same cycle period in both data sets, we indeed find spot dominance for most of the stars where a rotation period could be detected. That implies that a star can be spot-dominated on rotational time scales, whereas it can be faculae-dominated on activity cycle time scales.

6. Conclusion

In this paper we have determined activity cycle periods for 27 out of the 30 stars in our sample. By computing the phase difference between the photometric and the chromospheric time series we have shown that stellar activity transitions from spot to faculae domination at an activity level of $\log R'_{\text{HK}} \approx -4.75$. This value equals the activity level at the Vaughan-Preston gap. Using activity-rotation-age relations this activity level is associated with a Rossby number $Ro \approx 1$ and an age of ~ 2.55 Gyr. Furthermore, the transitional age of ~ 2.55 Gyr is consistent with measurements of a change of the activity cycle shape and the global magnetic field topology from the literature (Oláh et al. 2016; See et al. 2016). These results provide observational constraints on the underlying dynamo. The connection between the dominant source of surface activity and the magnetic field topology

sounds promising to either infer the type of surface activity from magnetic field measurements or vice versa.

We further conclude that the lack of intermediate active stars at the Vaughan-Preston gap cannot explain the dearth of intermediate rotation periods discovered by the *Kepler* telescope. Nevertheless, the results presented in this work strongly suggest that the importance of faculae contribution to the big picture of stellar activity has been underestimated so far. We propose a scenario to explain the dearth of rotation periods based on the cancellation of the spot and faculae contribution at rotation time scales. The proposed idea has been tested by simulating light curves with a solar faculae-to-spot ratio. We found that neither the periodogram nor the auto-correlation function were able to detect the correct rotation period. We plan to refine the light curve model, and extend it to stars of various spectral types in a forthcoming publication.

Acknowledgements. The research leading to the presented results has received funding from the European Research Council under the European Community's Seventh Framework Programme (2007-2013) / ERC grant agreement no 338251 (StellarAges). A.I.S. acknowledges the support by the European Research Council (ERC) under the European Unions Horizon 2020 research and innovation program (grant agreement no. 715947). We thank S. Messina and G. Lockwood and collaborators for kindly sharing their data with us. We also like to thank T. Metcalfe, H. Schunker, and R. H. Cameron for valuable discussion. The HK_Project_v1995_NSO data derived from the Mount Wilson Observatory HK Project, which was supported by both public and private funds through the Carnegie Observatories, the Mount Wilson Institute, and the Harvard-Smithsonian Center for Astrophysics starting in 1966 and continuing

for over 36 years. These data are the result of the dedicated work of O. Wilson, A. Vaughan, G. Preston, D. Duncan, S. Baliunas, and many others.

References

- Ambikasaran, S., Foreman-Mackey, D., Greengard, L., Hogg, D. W., & O’Neil, M. 2015, IEEE Transactions on Pattern Analysis and Machine Intelligence, 38 [arXiv:1403.6015]
- Angus, R., Morton, T., Aigrain, S., Foreman-Mackey, D., & Rajpaul, V. 2018, MNRAS, 474, 2094
- Balachandran, S. 1990, ApJ, 354, 310
- Baliunas, S., Sokoloff, D., & Soon, W. 1996, ApJ, 457, L99
- Baliunas, S. L., Donahue, R. A., Soon, W. H., et al. 1995, ApJ, 438, 269
- Barnes, S. A. 2007, ApJ, 669, 1167
- Barnes, S. A. 2010, ApJ, 722, 222
- Basri, G., Walkowicz, L. M., Batalha, N., et al. 2011, AJ, 141, 20
- Basri, G., Walkowicz, L. M., Batalha, N., et al. 2010, ApJ, 713, L155
- Baumann, I. & Solanki, S. K. 2005, A&A, 443, 1061
- Boeche, C. & Grebel, E. K. 2016, A&A, 587, A2
- Böhm-Vitense, E. 2007, ApJ, 657, 486
- Chen, Y. Q., Nissen, P. E., Zhao, G., Zhang, H. W., & Benoni, T. 2000, A&AS, 141, 491
- Davenport, J. R. A. 2017, ApJ, 835, 16
- Davenport, J. R. A. & Covey, K. R. 2018, ArXiv e-prints [arXiv:1807.09841]
- Duncan, D. K., Vaughan, A. H., Wilson, O. C., et al. 1991, ApJS, 76, 383
- Egeland, R., Soon, W., Baliunas, S., et al. 2017, ApJ, 835, 25
- Fliegge, M., Solanki, S. K., & Unruh, Y. C. 2000, A&A, 353, 380
- Foreman-Mackey, D., Hogg, D. W., Lang, D., & Goodman, J. 2013, PASP, 125, 306
- Goodman, J. & Weare, J. 2010, Communications in Applied Mathematics and Computational Science, Vol. 5, No. 1, p. 65-80, 2010, 5, 65
- König, B., Guenther, E. W., Woitas, J., & Hatzes, A. P. 2005, A&A, 435, 215
- Krivova, N. A., Solanki, S. K., Fligge, M., & Unruh, Y. C. 2003, A&A, 399, L1
- Lehtinen, J., Jetsu, L., Hackman, T., Kajatkari, P., & Henry, G. W. 2016, A&A, 588, A38
- Linsky, J. L., McClintock, W., Robertson, R. M., & Worden, S. P. 1979, ApJS, 41, 47
- Lockwood, G. W., Skiff, B. A., Henry, G. W., et al. 2007, ApJS, 171, 260
- Lockwood, G. W., Skiff, B. A., & Radick, R. R. 1997, ApJ, 485, 789
- Mamajek, E. E. & Hillenbrand, L. A. 2008, ApJ, 687, 1264
- Martinez Pillet, V., Moreno-Insertis, F., & Vazquez, M. 1993, A&A, 274, 521
- Mathur, S., García, R. A., Ballot, J., et al. 2014, A&A, 562, A124
- McQuillan, A., Aigrain, S., & Mazeh, T. 2013, MNRAS, 432, 1203
- McQuillan, A., Mazeh, T., & Aigrain, S. 2014, ApJS, 211, 24
- Messina, S. & Guinan, E. F. 2002, A&A, 393, 225
- Messina, S. & Guinan, E. F. 2003, A&A, 409, 1017
- Metcalfe, T. S., Egeland, R., & van Sadlers, J. 2016, ApJ, 826, L2
- Metcalfe, T. S. & van Sadlers, J. 2017, Sol. Phys., 292, 126
- Middelkoop, F. 1982, A&A, 107, 31
- Mishenina, T. V., Pignatari, M., Korotin, S. A., et al. 2013, A&A, 552, A128
- Montet, B. T., Tovar, G., & Foreman-Mackey, D. 2017, ApJ, 851, 116
- Morris, B. M., Agol, E., Hebb, L., & Hawley, S. L. 2018, AJ, 156, 91
- Niedzielski, A., Deka-Szymankiewicz, B., Adamczyk, M., et al. 2016, A&A, 585, A73
- Noyes, R. W., Hartmann, L. W., Baliunas, S. L., Duncan, D. K., & Vaughan, A. H. 1984, ApJ, 279, 763
- Olah, K., Kővári, Z., Petrovay, K., et al. 2016, A&A, 590, A133
- Olsperg, N., Lehtinen, J. J., Käpälä, M. J., Pelt, J., & Grigorievskiy, A. 2017, ArXiv e-prints [arXiv:1712.08240]
- Pettersen, B. R., Hawley, S. L., & Fisher, G. H. 1992, Sol. Phys., 142, 197
- Preminger, D. G., Chapman, G. A., & Cookson, A. M. 2011, ApJ, 739, L45
- Prugniel, P., Vauglin, I., & Koleva, M. 2011, A&A, 531, A165
- Radick, R. R., Lockwood, G. W., Henry, G. W., Hall, J. C., & Pevtsov, A. A. 2018, ApJ, 855, 75
- Radick, R. R., Lockwood, G. W., Skiff, B. A., & Baliunas, S. L. 1998, ApJS, 118, 239
- Ramírez, I., Allende Prieto, C., & Lambert, D. L. 2013, ApJ, 764, 78
- Ramírez, I., Michel, R., Sefako, R., et al. 2012, ApJ, 752, 5
- Rasmussen, C. E. & Williams, C. K. I. 2005, Gaussian Processes for Machine Learning (Adaptive Computation and Machine Learning) (The MIT Press)
- Reinhold, T., Cameron, R. H., & Gizon, L. 2017, A&A, 603, A52
- Reinhold, T. & Gizon, L. 2015, A&A, 583, A65
- Reinhold, T., Reiners, A., & Basri, G. 2013, A&A, 560, A4
- Rutten, R. G. M. 1984, A&A, 130, 353
- Saar, S. H. & Brandenburg, A. 1999, ApJ, 524, 295
- Saikia, S. B., Marvin, C. J., Jeffers, S. V., et al. 2018, A&A, 616, A108
- See, V., Jardine, M., Vidotto, A. A., et al. 2016, MNRAS, 462, 4442
- Shapiro, A. I., Solanki, S. K., Krivova, N. A., et al. 2017, Nature Astronomy, 1, 612
- Shapiro, A. I., Solanki, S. K., Krivova, N. A., et al. 2014, A&A, 569, A38
- Shapiro, A. I., Solanki, S. K., Krivova, N. A., Yeo, K. L., & Schmutz, W. K. 2016, A&A, 589, A46
- Skumanich, A. 1972, ApJ, 171, 565
- Takeda, Y. 2007, PASJ, 59, 335
- Vaughan, A. H. & Preston, G. W. 1980, PASP, 92, 385
- Vaughan, A. H., Preston, G. W., & Wilson, O. C. 1978, PASP, 90, 267
- Wilson, O. C. 1968, ApJ, 153, 221
- Wilson, O. C. 1978, ApJ, 226, 379
- Witzke, V., Shapiro, A. I., Solanki, S. K., Krivova, N. A., & Schmutz, W. 2018, ArXiv e-prints [arXiv:1809.04360]
- Zechmeister, M. & Kürster, M. 2009, A&A, 496, 577

Appendix A: Photometric data

Table A.1. HD 1835 photometric observing seasons (in JD-2440000).

JD range	N _{obs}	JD _{mean}	Δ(b + y)/2 _{mean}	σ _{by}
5949.83–6078.77	30	6034.32	-0.0064	0.0088
6287.86–6433.77	53	6348.44	0.0059	0.0102
6642.86–6778.77	38	6714.40	-0.0039	0.0088
7037.85–7137.78	27	7084.78	0.0048	0.0064
7419.84–7528.77	34	7472.45	0.0167	0.0064
7770.84–7836.80	32	7800.20	0.0062	0.0120
8125.85–8230.78	38	8170.29	0.0134	0.0099
8514.84–8598.78	22	8544.36	-0.0075	0.0067
8863.85–8992.77	38	8913.08	-0.0088	0.0084
9215.85–9353.60	37	9294.45	-0.0057	0.0184
9547.00–9706.60	57	9647.00	-0.0111	0.0119
9974.83–10087.60	47	10009.30	0.0035	0.0073
10307.86–10458.60	37	10390.79	0.0020	0.0075
10712.83–10799.60	38	10742.73	0.0078	0.0054
11072.83–11197.60	60	11127.88	-0.0087	0.0078
11450.80–11549.60	55	11490.14	-0.0109	0.0101
11809.80–11928.60	30	11862.86	0.0017	0.0074
12193.70–12283.60	19	12239.49	0.0018	0.0092
12533.80–12658.60	36	12597.38	0.0149	0.0070

Table A.2. HD 10476 photometric observing seasons (in JD-2440000).

JD range	N _{obs}	JD _{mean}	Δ(b + y)/2 _{mean}	σ _{by}
5949.83–6069.77	32	6016.92	0.0032	0.0014
6294.86–6425.79	30	6365.41	0.0032	0.0013
6658.87–6808.77	28	6713.82	-0.0008	0.0015
7039.85–7158.77	30	7094.75	-0.0002	0.0012
7419.84–7535.77	32	7469.50	-0.0004	0.0015
7771.85–7853.80	40	7816.02	-0.0027	0.0017
8125.85–8230.79	36	8175.15	-0.0025	0.0011
8514.84–8598.78	18	8545.38	-0.0021	0.0009
8863.86–8929.80	28	8891.69	-0.0017	0.0009
9215.86–9389.60	58	9309.29	-0.0002	0.0013
9595.86–9751.60	46	9647.90	-0.0000	0.0014
9976.83–10123.60	53	10025.85	0.0000	0.0013
10348.83–10494.60	47	10396.72	0.0009	0.0013
10715.84–10856.60	43	10765.05	0.0007	0.0017
11072.84–11218.60	69	11128.76	0.0011	0.0016
11435.00–11577.70	77	11495.25	-0.0002	0.0017
11807.00–11962.60	40	11867.40	-0.0005	0.0018
12196.80–12328.60	27	12261.18	-0.0002	0.0011
12533.90–12673.70	40	12606.90	0.0004	0.0017

Appendix B: Mount Wilson data

Appendix C: Example light curves

Table A.3. HD 13421 photometric observing seasons (in JD-2440000).

JD range	N _{obs}	JD _{mean}	Δ(b + y)/2 _{mean}	σ _{by}
5956.84–6066.78	24	6010.06	0.0019	0.0023
6307.86–6451.77	18	6382.03	0.0018	0.0018
6679.86–6809.77	29	6732.89	0.0006	0.0020
7039.86–7173.77	17	7104.99	-0.0007	0.0017
7419.85–7546.77	22	7479.63	-0.0004	0.0015
7793.84–7884.78	26	7840.58	-0.0012	0.0022
8147.85–8218.80	15	8186.22	-0.0005	0.0013
8532.84–8598.79	12	8556.66	0.0003	0.0013
8867.86–8977.78	14	8910.97	0.0001	0.0014
9248.80–9389.60	40	9324.31	-0.0003	0.0012
9595.87–9751.60	46	9657.35	-0.0001	0.0014
9977.84–10130.60	59	10039.30	-0.0005	0.0013
10348.84–10486.60	48	10397.22	-0.0001	0.0013
10715.84–10861.60	48	10775.12	0.0009	0.0012
11085.90–11223.60	70	11146.90	-0.0007	0.0016
11435.00–11595.60	75	11507.73	0.0009	0.0012
11807.90–11959.60	46	11876.82	0.0007	0.0013
12179.90–12314.60	23	12255.73	-0.0020	0.0010
12533.90–12692.60	27	12612.88	-0.0023	0.0013

Table A.4. HD 18256 photometric observing seasons (in JD-2440000).

JD range	N _{obs}	JD _{mean}	Δ(b + y)/2 _{mean}	σ _{by}
5956.84–6083.78	18	6016.37	0.0021	0.0019
6307.86–6460.78	19	6390.71	0.0019	0.0013
6680.86–6809.78	15	6740.82	0.0001	0.0016
7064.85–7173.78	15	7118.28	-0.0005	0.0014
7524.80–7556.77	10	7537.19	-0.0003	0.0005
7824.82–7884.79	20	7848.81	-0.0015	0.0024
8125.86–8219.80	16	8176.33	-0.0003	0.0011
8533.83–8598.80	8	8551.83	-0.0030	0.0015
8863.86–8989.78	20	8912.83	-0.0003	0.0011
9239.90–9399.60	80	9318.09	0.0004	0.0013
9611.86–9769.60	64	9669.54	-0.0001	0.0013
9980.85–10122.60	69	10029.47	-0.0006	0.0014
10348.85–10511.60	46	10395.42	-0.0018	0.0018
10719.00–10861.70	38	10766.19	-0.0019	0.0015
11086.90–11222.70	54	11144.28	0.0017	0.0010
11447.80–11582.70	66	11505.95	-0.0012	0.0015
11808.00–11956.70	37	11876.75	0.0007	0.0012
12200.90–12342.60	26	12261.84	0.0029	0.0013
12533.90–12692.70	39	12604.36	0.0014	0.0014

Table A.5. HD 20630 photometric observing seasons (in JD-2440000).

JD range	N _{obs}	JD _{mean}	V _{mean}	σ _V
7908.21–8301.29	29	8166.21	4.8458	0.0121
8435.31–9031.42	41	8606.20	4.8405	0.0123
9239.92–9393.66	87	9309.28	4.8182	0.0079
9624.92–9773.60	60	9676.74	4.8209	0.0058
9986.90–10123.64	50	10036.29	4.8429	0.0065
10391.93–10482.70	32	10436.63	4.8459	0.0132
10718.95–10836.71	27	10764.94	4.8399	0.0065
11102.94–11240.61	33	11160.70	4.8258	0.0068

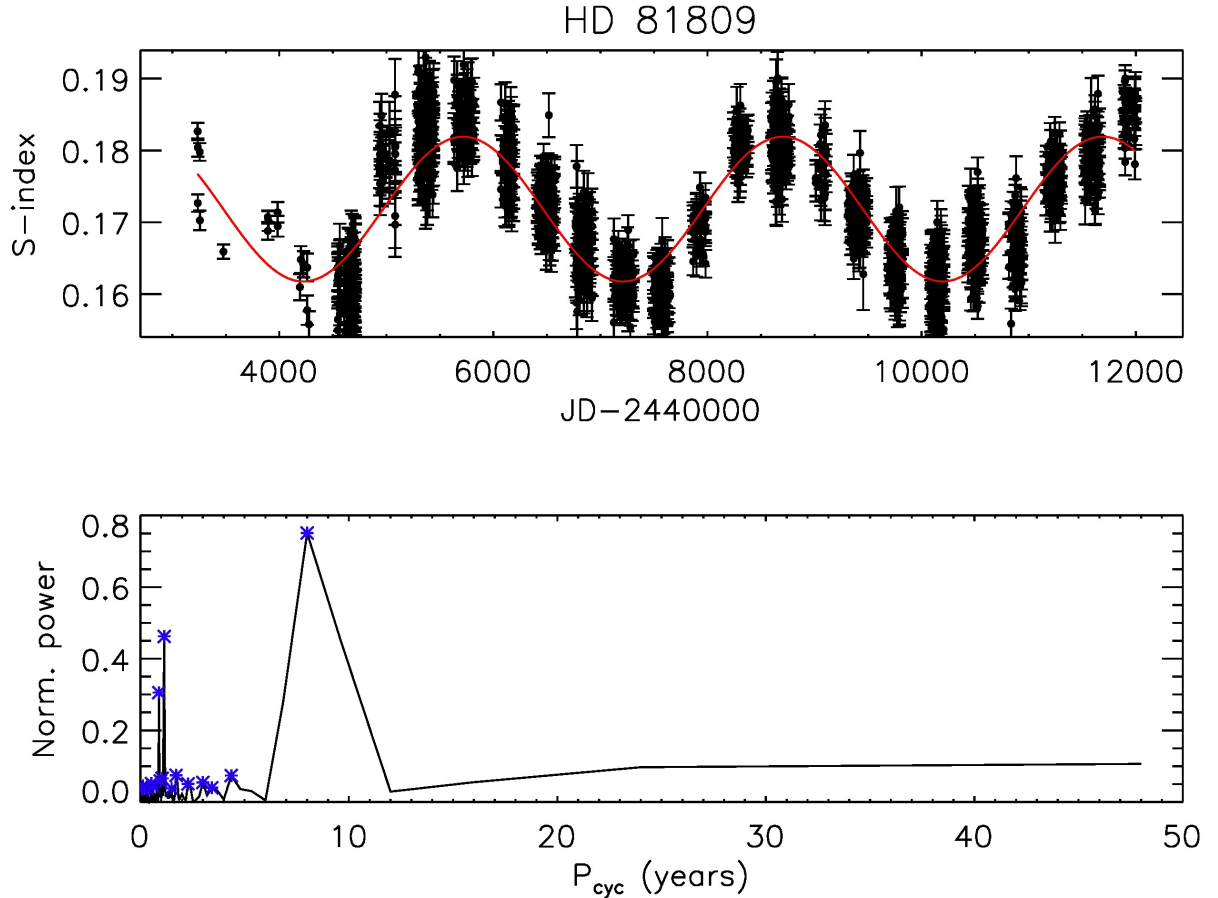


Fig. C.1. Top panel: Chromospheric time series of the star HD 81809 flagged as excellent periodicity ($\text{flag}_{\text{chrom}} = 3$). The red curve shows the best sine fit to the data. Bottom panel: Lomb-Scargle periodogram of the time series.

Table A.6. HD 25998 photometric observing seasons (in JD-2440000).

JD range	N _{obs}	JD _{mean}	$\Delta(b + y)/2_{\text{mean}}$	σ_{by}
5956.86–6087.78	16	6043.69	0.0013	0.0057
6331.86–6433.80	21	6381.40	0.0018	0.0027
6679.86–6828.80	23	6736.87	-0.0033	0.0040
7069.85–7173.78	10	7126.42	-0.0030	0.0039
7524.81–7530.81	6	7527.47	0.0037	0.0033
7837.84–7933.79	12	7882.31	-0.0001	0.0053
8206.82–8276.80	12	8225.14	-0.0004	0.0038
8534.84–8632.78	8	8576.06	-0.0022	0.0079
8889.85–9000.80	8	8949.32	0.0018	0.0029
9326.81–9385.79	16	9350.55	0.0019	0.0038
9611.86–9687.80	24	9650.83	0.0003	0.0048
9991.85–10098.79	26	10043.58	-0.0038	0.0054
10348.86–10395.83	24	10365.59	0.0053	0.0032

Table A.7. HD 35296 photometric observing seasons (in JD-2440000).

JD range	N _{obs}	JD _{mean}	$\Delta(b + y)/2_{\text{mean}}$	σ_{by}
5761.79–5779.78	10	5770.38	0.0006	0.0041
5956.86–6150.79	30	6089.81	0.0037	0.0072
6331.87–6513.78	63	6421.10	-0.0013	0.0068
6705.88–6882.78	32	6777.12	-0.0071	0.0057
7104.85–7234.78	33	7179.26	0.0029	0.0083
7523.82–7607.78	24	7563.55	0.0042	0.0055
7844.84–7973.78	26	7918.34	-0.0020	0.0076
8218.84–8313.78	14	8262.52	-0.0014	0.0054
8598.83–8698.78	20	8645.00	0.0025	0.0050
8928.85–9055.78	16	8985.32	0.0021	0.0081
9326.82–9396.80	19	9357.18	-0.0022	0.0067
9634.86–9688.83	24	9663.68	0.0041	0.0040
10008.85–10102.80	24	10051.41	0.0030	0.0059
10367.86–10519.78	24	10470.97	-0.0030	0.0055
10884.78–10892.78	6	10889.11	-0.0120	0.0061
11212.78–11248.78	4	11230.78	0.0005	0.0010
11525.81–11579.79	8	11556.30	0.0039	0.0011

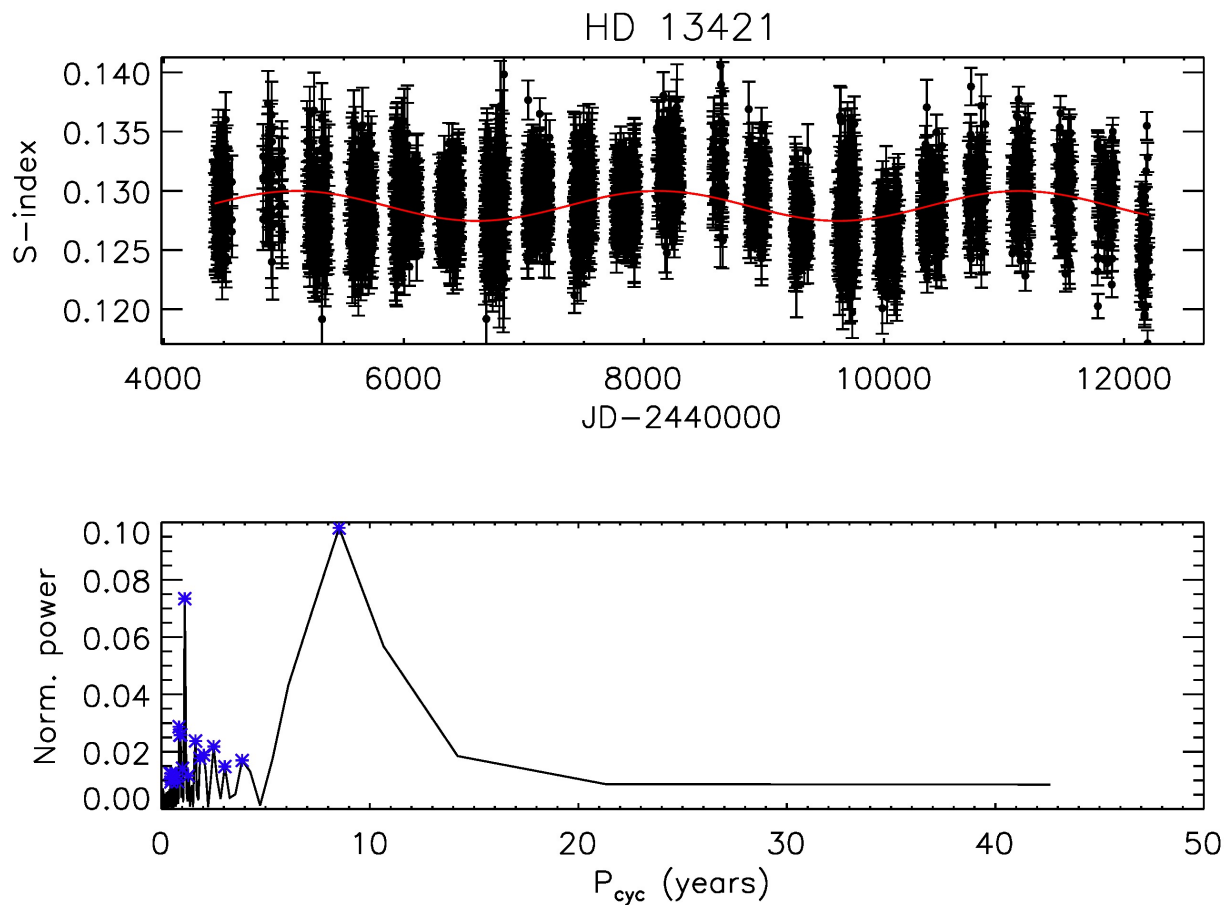


Fig. C.2. Top panel: Chromospheric time series of the star HD 13421 flagged as weak periodicity ($\text{flag}_{\text{chrom}} = 1$). The red curve shows the best sine fit to the data. Bottom panel: Lomb-Scargle periodogram of the time series.

Table A.8. HD 39587 photometric observing seasons (in JD-2440000).

JD range	N _{obs}	JD _{mean}	$\Delta(b + y)/2_{\text{mean}}$	σ_{by}
5761.79–5779.78	10	5770.38	0.0140	0.0019
5956.86–6150.79	30	6089.81	0.0065	0.0068
6331.87–6513.78	63	6421.10	0.0004	0.0057
6705.88–6882.78	32	6777.12	-0.0006	0.0059
7104.85–7234.78	33	7179.26	-0.0032	0.0062
7523.82–7607.78	24	7563.55	-0.0016	0.0054
7844.84–7973.78	26	7918.34	-0.0072	0.0062
8218.84–8313.78	12	8266.81	0.0004	0.0015
8598.83–8698.78	20	8645.00	-0.0051	0.0059
8928.85–9055.78	16	8985.32	-0.0071	0.0094
9326.82–9396.80	19	9357.18	0.0045	0.0042
9634.86–9688.83	24	9663.68	0.0048	0.0060
10008.85–10102.80	24	10051.41	0.0075	0.0062
10367.86–10519.78	24	10470.97	-0.0009	0.0082
10884.78–10892.78	6	10889.11	-0.0062	0.0043
11183.80–11248.78	6	11215.12	-0.0057	0.0062
11525.81–11579.79	8	11556.30	-0.0087	0.0030

Table A.9. HD 72905 photometric observing seasons (in JD-2440000).

JD range	N _{obs}	JD _{mean}	V _{mean}	σ_V
7625.66–7650.69	15	7638.21	5.6785	0.0066
7815.03–8024.19	57	7917.05	5.6734	0.0087
8133.73–8492.62	116	8302.56	5.6755	0.0103
8560.34–8765.22	60	8677.77	5.6809	0.0085
8972.11–9062.71	22	9027.58	5.6691	0.0074
9284.98–9482.65	122	9368.75	5.6472	0.0089
9645.00–9808.77	94	9725.89	5.6529	0.0094
10029.95–10214.65	94	10131.35	5.6471	0.0067
10405.99–10569.68	81	10484.01	5.6519	0.0064
10736.02–10949.65	102	10848.40	5.6351	0.0049
11118.97–11317.66	82	11225.23	5.6509	0.0065
11546.81–11634.68	31	11584.92	5.6535	0.0069

Table A.10. HD 75332 photometric observing seasons (in JD-2440000).

JD range	N _{obs}	JD _{mean}	$\Delta(b+y)/2_{\text{mean}}$	σ_{by}
6363.44–6517.79	34	6433.53	0.0033	0.0048
6741.87–6906.79	29	6848.85	-0.0150	0.0105
7149.84–7239.79	32	7208.00	-0.0078	0.0058
7525.84–7627.79	29	7575.99	0.0008	0.0037
7917.82–7992.79	20	7949.91	0.0020	0.0044
8276.83–8324.81	12	8297.32	-0.0013	0.0026
8632.83–8719.78	22	8661.64	0.0027	0.0027
8928.86–9124.70	20	9049.63	0.0080	0.0044
9287.00–9475.70	94	9377.07	0.0024	0.0045
9663.00–9832.70	70	9748.82	0.0071	0.0032
10030.00–10218.70	47	10125.57	0.0008	0.0051
10404.90–10577.70	47	10484.15	-0.0064	0.0046
10737.00–10956.70	53	10859.31	-0.0023	0.0044
11093.00–11314.70	42	11208.17	-0.0060	0.0060
11471.00–11668.70	47	11574.77	-0.0007	0.0040
11833.00–12046.70	55	11963.18	-0.0040	0.0074
12216.00–12422.70	53	12317.58	0.0062	0.0034
12567.00–12785.70	65	12684.54	0.0025	0.0057

Table A.11. HD 81809 photometric observing seasons (in JD-2440000).

JD range	N _{obs}	JD _{mean}	$\Delta(b+y)/2_{\text{mean}}$	σ_{by}
5763.79–5815.79	21	5789.41	-0.0000	0.0024
6065.85–6159.79	26	6123.74	0.0011	0.0024
6404.44–6512.81	14	6465.66	0.0004	0.0017
6808.84–6908.78	28	6865.67	-0.0037	0.0025
7198.83–7251.80	33	7220.84	-0.0009	0.0019
7536.85–7627.79	21	7578.06	-0.0005	0.0020
7920.83–8008.79	20	7959.01	-0.0008	0.0024
8276.84–8378.79	14	8322.10	-0.0013	0.0015
8637.84–8733.79	22	8675.00	-0.0000	0.0027
9021.83–9121.60	17	9076.07	-0.0013	0.0030
9295.00–9482.60	97	9386.77	0.0008	0.0020
9662.00–9840.70	98	9749.32	0.0002	0.0019
10030.00–10213.60	64	10122.37	-0.0007	0.0016
10406.00–10552.70	56	10490.81	0.0009	0.0015
10761.00–10944.70	49	10863.14	-0.0003	0.0015
11124.00–11315.70	39	11225.24	-0.0009	0.0025
11479.00–11669.70	54	11572.73	0.0017	0.0014
11865.00–12036.70	44	11957.70	0.0006	0.0018
12245.90–12403.70	40	12305.69	0.0008	0.0018
12574.00–12771.70	50	12666.29	-0.0006	0.0019

Table A.12. HD 82443 photometric observing seasons (in JD-2440000).

JD range	N _{obs}	JD _{mean}	V _{mean}	σ_V
7570.82–7673.66	63	7617.97	7.0558	0.0243
7976.36–8065.31	35	8031.52	7.0455	0.0165
8193.90–8393.43	32	8312.40	7.0633	0.0243
8540.72–8761.57	53	8667.59	7.0848	0.0274
8906.01–9137.65	110	9030.65	7.0516	0.0117
9284.96–9511.65	208	9416.95	7.0478	0.0128
9644.97–9840.69	126	9741.10	7.0667	0.0234
9996.02–10216.71	145	10104.08	7.0639	0.0247
10392.92–10575.69	240	10497.37	7.0496	0.0214
10728.01–10976.65	160	10857.47	7.0641	0.0184
11094.00–11303.70	142	11203.53	7.0583	0.0139
11546.91–11612.79	17	11568.05	7.0412	0.0145

Table A.13. HD 82885 photometric observing seasons (in JD-2440000).

JD range	N _{obs}	JD _{mean}	$\Delta(b+y)/2_{\text{mean}}$	σ_{by}
5763.80–5815.79	22	5792.34	0.0061	0.0063
6065.86–6197.79	54	6138.66	-0.0039	0.0127
6373.88–6571.79	55	6487.74	0.0019	0.0053
6741.44–6921.79	41	6865.83	0.0031	0.0034
7199.84–7259.79	38	7218.82	0.0088	0.0026
7536.84–7665.79	34	7597.17	0.0074	0.0040
7917.83–8023.79	32	7973.43	0.0043	0.0043
8276.84–8382.79	24	8338.81	0.0055	0.0035
8632.84–8733.79	22	8670.46	0.0006	0.0027
9021.82–9139.60	35	9090.83	0.0062	0.0037
9298.00–9486.70	119	9397.43	-0.0020	0.0060
9675.00–9870.60	100	9757.83	-0.0024	0.0060
10030.00–10223.70	95	10134.76	0.0024	0.0041
10404.90–10600.60	81	10490.79	-0.0012	0.0054
10737.00–10959.70	75	10869.01	-0.0037	0.0093
11094.00–11325.70	60	11229.36	0.0056	0.0035
11471.00–11690.70	84	11593.82	0.0000	0.0067
11833.00–12060.70	55	11962.38	-0.0001	0.0049
12216.00–12425.70	65	12330.08	-0.0121	0.0068
12567.00–12786.70	79	12687.88	-0.0018	0.0058

Table A.14. HD 103095 photometric observing seasons (in JD-2440000).

JD range	N _{obs}	JD _{mean}	$\Delta(b+y)/2_{\text{mean}}$	σ_{by}
5763.82–5838.79	20	5796.60	0.0007	0.0014
6065.87–6165.80	28	6120.69	-0.0009	0.0011
6421.86–6540.79	21	6497.30	0.0011	0.0014
6809.86–6920.80	20	6873.52	0.0014	0.0025
7199.85–7247.81	34	7219.66	0.0013	0.0016
7543.86–7667.80	26	7624.81	0.0013	0.0013
7967.82–8032.79	26	8006.34	0.0017	0.0017
8276.85–8390.79	28	8343.82	0.0016	0.0019
8637.86–8756.79	16	8719.94	0.0007	0.0020
9021.84–9164.70	62	9115.47	-0.0014	0.0020
9317.00–9528.70	125	9426.35	-0.0019	0.0014
9689.00–9891.70	114	9791.35	-0.0012	0.0014
10052.00–10251.70	98	10145.47	-0.0009	0.0013
10405.00–10633.70	97	10522.94	-0.0005	0.0014
10762.00–10996.70	104	10903.46	0.0008	0.0015
11149.00–11354.70	76	11264.31	0.0012	0.0021
11504.00–11709.70	95	11621.09	0.0011	0.0016
11862.00–12076.70	77	11998.97	0.0009	0.0013
12246.00–12446.70	75	12348.87	0.0002	0.0017
12601.00–12813.70	76	12709.92	0.0001	0.0015

Table A.15. HD 115383 photometric observing seasons (in JD-2440000).

JD range	N _{obs}	JD _{mean}	$\Delta(b + y)/2_{\text{mean}}$	σ_{by}
5781.83–5840.80	11	5802.55	-0.0095	0.0014
6104.86–6226.79	12	6157.33	0.0016	0.0046
6487.85–6571.81	21	6521.60	0.0059	0.0027
6881.84–6965.79	9	6908.71	0.0008	0.0023
7200.86–7320.80	28	7263.90	-0.0049	0.0041
7602.84–7697.79	18	7649.81	0.0062	0.0039
8008.80–8061.80	18	8042.58	0.0030	0.0044
8301.85–8405.80	22	8368.36	-0.0045	0.0025
8732.82–8785.79	10	8757.80	-0.0064	0.0027
9052.84–9164.70	62	9127.20	0.0003	0.0056
9339.00–9546.70	75	9460.55	-0.0020	0.0041
9718.00–9908.70	93	9819.91	0.0054	0.0035
10071.00–10249.70	79	10175.46	0.0001	0.0032
10434.00–10635.70	89	10540.95	-0.0010	0.0032
10795.00–10993.70	109	10909.06	-0.0065	0.0045
11181.00–11344.70	52	11287.39	-0.0048	0.0033
11530.00–11710.79	67	11631.35	-0.0004	0.0048
11888.00–12075.70	33	11998.83	0.0026	0.0051
12263.10–12462.70	68	12356.41	0.0081	0.0037
12616.00–12829.70	65	12725.22	0.0021	0.0039

Table A.16. HD 115404 photometric observing seasons (in JD-2440000).

JD range	N _{obs}	JD _{mean}	$\Delta(b + y)/2_{\text{mean}}$	σ_{by}
5781.84–5850.80	18	5824.93	-0.0167	0.0052
6104.86–6235.79	39	6190.82	-0.0081	0.0062
6487.84–6571.81	25	6518.20	-0.0021	0.0086
6881.84–6969.79	11	6913.64	-0.0074	0.0083
7215.85–7320.80	22	7269.27	-0.0082	0.0031
7602.85–7705.80	18	7652.48	-0.0072	0.0077
8008.81–8066.80	20	8045.00	-0.0075	0.0077
8328.85–8405.80	21	8374.15	-0.0082	0.0079
8716.83–8786.79	9	8754.14	-0.0018	0.0015
9066.85–9164.70	64	9126.91	-0.0071	0.0053
9335.00–9540.70	99	9440.05	-0.0071	0.0104
9725.00–9908.70	75	9809.45	0.0021	0.0049
10063.00–10265.70	64	10172.32	0.0042	0.0047
10419.00–10635.70	76	10535.51	0.0083	0.0080
10788.00–10993.70	75	10899.02	0.0006	0.0068
11149.00–11360.70	60	11275.34	0.0028	0.0065
11531.00–11709.80	61	11638.53	0.0022	0.0066
11888.00–12076.70	62	12008.56	0.0024	0.0062
12246.00–12447.70	54	12350.97	0.0079	0.0053
12618.00–12813.70	65	12722.58	0.0097	0.0052

Table A.17. HD 120136 photometric observing seasons (in JD-2440000).

JD range	N _{obs}	JD _{mean}	$\Delta(b + y)/2_{\text{mean}}$	σ_{by}
5777.83–5865.80	24	5831.81	0.0054	0.0023
6104.87–6238.79	16	6181.95	0.0045	0.0016
6487.85–6595.80	15	6547.09	-0.0030	0.0041
6883.84–6970.79	16	6933.75	-0.0045	0.0016
7200.44–7320.81	26	7267.51	-0.0024	0.0022
7602.85–7704.80	18	7663.37	-0.0035	0.0014
8019.81–8064.80	18	8045.91	-0.0042	0.0017
8356.83–8425.80	16	8387.19	-0.0036	0.0015
8733.83–8801.80	11	8773.98	-0.0029	0.0010
9079.84–9164.70	61	9129.00	-0.0008	0.0026
9345.00–9547.70	83	9460.59	-0.0002	0.0013
9725.00–9890.70	81	9824.10	0.0010	0.0019
10085.00–10241.80	76	10177.83	0.0005	0.0013
10436.00–10635.70	254	10553.47	-0.0004	0.0015
10795.00–10993.70	83	10913.88	0.0015	0.0017
11182.00–11342.80	57	11290.73	0.0015	0.0014
11531.00–11729.70	63	11640.16	0.0015	0.0016
11894.00–12076.80	43	12012.53	0.0025	0.0017
12268.00–12448.70	41	12356.12	-0.0011	0.0016
12650.00–12829.70	45	12736.26	-0.0027	0.0020

Table A.18. HD 124570 photometric observing seasons (in JD-2440000).

JD range	N _{obs}	JD _{mean}	$\Delta(b + y)/2_{\text{mean}}$	σ_{by}
5777.84–5865.80	16	5815.45	-0.0037	0.0017
6145.84–6226.80	19	6190.40	-0.0032	0.0009
6487.86–6602.80	29	6550.58	-0.0017	0.0015
6883.85–6970.79	14	6931.74	-0.0014	0.0021
7204.87–7349.80	18	7271.83	-0.0016	0.0011
7630.82–7709.80	20	7675.71	-0.0016	0.0011
8008.82–8065.80	18	8044.36	-0.0018	0.0020
8369.83–8405.80	16	8388.69	-0.0013	0.0016
8755.82–8800.79	10	8782.60	-0.0003	0.0013
9094.80–9164.70	27	9133.34	-0.0003	0.0010
9354.00–9519.70	30	9465.50	-0.0006	0.0010
9747.00–9890.70	42	9830.80	0.0005	0.0012
10122.00–10249.70	28	10184.23	0.0005	0.0012
10435.00–10635.70	53	10540.62	0.0009	0.0017
10798.00–10994.70	61	10909.38	0.0011	0.0017
11178.00–11342.80	49	11288.36	0.0014	0.0013
11531.00–11710.80	61	11640.99	0.0024	0.0015
11895.00–12084.80	54	12019.94	0.0009	0.0013
12263.00–12462.70	72	12364.38	-0.0005	0.0009
12629.00–12829.70	91	12735.89	-0.0006	0.0010

Table A.19. HD 129333 photometric observing seasons (in JD-2440000).

JD range	N _{obs}	JD _{mean}	$\Delta(b + y)/2_{\text{mean}}$	σ_{by}
5781.86–5874.80	14	5843.96	0.0728	0.0146
6104.47–6252.79	54	6211.03	0.0722	0.0204
6488.03–6640.79	52	6555.81	0.0519	0.0136
6829.87–6983.80	26	6937.55	0.0143	0.0161
7199.86–7348.80	36	7256.06	0.0223	0.0137
7580.84–7725.79	44	7668.11	0.0179	0.0164
8008.82–8066.80	40	8039.91	0.0214	0.0168
8369.84–8439.80	35	8399.53	0.0067	0.0252
8732.83–8806.79	26	8775.70	0.0214	0.0142
9030.86–9163.70	72	9127.20	0.0077	0.0234
9357.00–9548.79	84	9468.00	0.0274	0.0232
9725.00–9908.70	95	9828.22	0.0032	0.0326
10087.00–10260.70	93	10186.45	-0.0026	0.0288
10480.00–10639.79	46	10567.82	-0.0089	0.0440
10800.00–10996.70	59	10919.59	-0.0279	0.0196
11176.00–11342.80	55	11276.69	-0.0491	0.0272
11557.00–11709.80	54	11646.17	-0.0561	0.0288
11962.00–12074.80	44	12027.82	-0.0416	0.0379
12281.00–12447.80	33	12378.15	-0.0682	0.0216
12636.00–12811.80	46	12734.45	-0.0476	0.0244

Table A.20. HD 131156A photometric observing seasons (in JD-2440000).

JD range	N _{obs}	JD _{mean}	$\Delta(b + y)/2_{\text{mean}}$	σ_{by}
5777.84–5874.80	28	5840.46	-0.0023	0.0065
6105.18–6251.80	43	6205.60	-0.0013	0.0058
6487.86–6602.80	33	6554.10	0.0016	0.0074
6882.87–6980.80	35	6943.67	0.0047	0.0075
7232.86–7349.80	16	7288.83	-0.0160	0.0032
7627.84–7708.79	33	7676.06	0.0053	0.0055
8008.83–8066.80	32	8045.06	0.0033	0.0100
8381.84–8416.81	14	8394.11	0.0102	0.0022
8732.84–8806.80	25	8782.37	0.0011	0.0057
9107.83–9139.80	23	9125.69	0.0120	0.0086
9443.86–9546.79	24	9498.40	-0.0062	0.0056
9800.85–9892.80	24	9848.24	-0.0154	0.0063
10161.86–10233.80	24	10194.42	-0.0136	0.0060
10571.82–10629.79	26	10618.34	0.0106	0.0085

Table A.21. HD 143761 photometric observing seasons (in JD-2440000).

JD range	N _{obs}	JD _{mean}	$\Delta(b + y)/2_{\text{mean}}$	σ_{by}
5783.86–5867.81	22	5839.83	-0.0035	0.0018
6145.86–6223.82	18	6194.72	-0.0024	0.0012
6487.87–6602.81	18	6553.48	-0.0022	0.0010
6885.86–6976.80	19	6942.82	-0.0019	0.0011
7284.84–7320.82	8	7301.58	-0.0019	0.0017
7644.84–7723.79	34	7693.22	-0.0009	0.0015
8016.83–8065.81	32	8050.00	-0.0010	0.0014
8381.84–8382.84	4	8382.34	-0.0003	0.0015
8732.84–8803.80	22	8778.45	-0.0003	0.0015
9094.85–9163.82	72	9129.31	-0.0006	0.0012
9372.05–9547.76	80	9476.56	-0.0005	0.0010
9750.02–9923.80	97	9845.46	-0.0004	0.0013
10109.04–10265.76	76	10190.36	-0.0003	0.0012
10466.01–10631.83	83	10578.93	0.0006	0.0014
10823.03–11000.79	163	10948.59	0.0004	0.0018
11184.04–11362.79	67	11309.71	0.0014	0.0017
11557.03–11711.80	62	11650.55	0.0020	0.0013
11941.97–12076.84	47	12028.41	0.0018	0.0018

Table A.22. HD 149661 photometric observing seasons (in JD-2440000).

JD range	N _{obs}	JD _{mean}	$\Delta(b + y)/2_{\text{mean}}$	σ_{by}
5781.87–5874.81	18	5842.27	-0.0101	0.0058
6145.87–6251.80	26	6224.43	-0.0070	0.0063
6567.84–6644.79	20	6612.61	-0.0013	0.0053
6909.86–6982.80	20	6966.41	-0.0106	0.0039
7644.85–7725.80	21	7697.05	-0.0089	0.0071
8016.84–8066.81	26	8047.98	-0.0060	0.0053
8399.83–8474.79	13	8430.43	-0.0036	0.0042
8756.84–8825.79	27	8796.00	-0.0013	0.0029
9096.90–9164.80	52	9138.90	0.0043	0.0067
9399.00–9547.70	65	9487.34	0.0015	0.0063
9774.00–9924.80	82	9864.26	0.0015	0.0069
10122.00–10260.70	68	10205.23	0.0018	0.0052
10490.00–10639.80	51	10591.16	0.0035	0.0048
10847.00–10996.70	41	10929.11	0.0088	0.0029
11224.00–11342.90	42	11299.85	-0.0016	0.0060
11591.00–11707.80	32	11652.68	-0.0088	0.0030
11960.00–12076.90	36	12030.87	-0.0038	0.0050
12400.90–12539.60	22	12433.23	0.0081	0.0036
12706.00–12811.90	34	12766.44	0.0089	0.0032

Table A.23. HD 158614 photometric observing seasons (in JD-2440000).

JD range	N _{obs}	JD _{mean}	$\Delta(b + y)/2_{\text{mean}}$	σ_{by}
5808.86–5874.82	14	5851.69	0.0039	0.0019
6197.84–6245.81	14	6229.11	0.0041	0.0016
6567.84–6625.80	12	6593.16	-0.0016	0.0025
6909.86–6983.81	18	6966.04	-0.0006	0.0017
7310.84–7384.79	6	7359.81	0.0003	0.0017
7702.82–7727.80	12	7714.31	-0.0007	0.0027
8016.84–8112.79	20	8052.63	-0.0026	0.0008
8410.83–8474.80	12	8437.48	-0.0018	0.0014
8756.84–8825.80	28	8793.04	-0.0006	0.0019
9130.84–9157.82	20	9145.33	-0.0007	0.0019
9483.84–9530.81	24	9509.33	-0.0001	0.0019
9862.84–9924.80	29	9896.25	-0.0000	0.0017
10193.86–10259.81	24	10237.49	0.0008	0.0019
10611.82–10639.80	18	10625.26	-0.0000	0.0018
10949.84–11011.80	20	10987.01	0.0004	0.0019
11361.80–11362.80	4	11362.30	0.0010	0.0013

Table A.24. HD 161239 photometric observing seasons (in JD-2440000).

JD range	N _{obs}	JD _{mean}	$\Delta(b + y)/2_{\text{mean}}$	σ_{by}
5808.86–5958.78	22	5885.05	0.0015	0.0046
6193.84–6278.80	30	6229.50	0.0012	0.0020
6517.86–6692.79	21	6613.30	-0.0017	0.0020
6908.85–6983.82	12	6959.49	-0.0004	0.0015
7289.84–7428.78	12	7376.47	0.0002	0.0012
7667.84–7793.78	14	7755.80	0.0027	0.0019
8028.84–8126.79	15	8062.43	0.0005	0.0026
8410.84–8437.84	4	8424.34	-0.0025	0.0025
8776.84–8827.82	18	8799.49	-0.0012	0.0025
9116.85–9170.83	22	9152.47	-0.0015	0.0016
9473.85–9529.84	24	9507.34	0.0006	0.0014
9812.86–9924.81	41	9880.83	-0.0009	0.0026
10167.87–10255.83	24	10225.17	0.0011	0.0033
10617.83–10639.81	16	10624.69	-0.0033	0.0018
10972.84–11045.79	20	11001.21	0.0027	0.0052
11331.82–11425.78	7	11358.38	-0.0030	0.0007

Table A.25. HD 182572 photometric observing seasons (in JD-2440000).

JD range	N _{obs}	JD _{mean}	$\Delta(b + y)/2_{\text{mean}}$	σ_{by}
5862.84–5996.77	28	5938.52	0.0021	0.0020
6219.85–6326.78	21	6250.92	0.0011	0.0014
6592.85–6719.77	22	6635.60	0.0014	0.0017
6957.84–7072.78	25	7005.94	0.0019	0.0019
7310.86–7425.79	12	7381.48	-0.0004	0.0013
7741.81–7800.78	22	7777.16	0.0006	0.0013
8066.84–8175.77	20	8131.90	-0.0002	0.0012
8824.82–8873.80	8	8848.06	0.0014	0.0018
9095.00–9301.60	95	9174.20	0.0016	0.0014
9443.00–9654.60	71	9536.42	0.0000	0.0015
9806.00–10017.60	60	9911.08	0.0000	0.0013
10173.00–10365.77	49	10266.27	0.0005	0.0018
10528.00–10777.60	72	10676.21	0.0000	0.0014
10897.00–11138.60	92	11021.03	-0.0007	0.0014
11262.00–11507.60	67	11400.17	-0.0015	0.0015
11621.00–11874.60	50	11720.52	-0.0023	0.0016
11986.00–12076.90	31	12044.77	-0.0012	0.0014
12179.60–12228.60	7	12215.03	-0.0000	0.0008
12401.00–12576.60	48	12467.52	-0.0008	0.0012
12737.00–12813.90	25	12770.86	0.0004	0.0014

Table A.26. HD 185144 photometric observing seasons (in JD-2440000).

JD range	N _{obs}	JD _{mean}	$\Delta(b + y)/2_{\text{mean}}$	σ_{by}
5862.85–5993.77	29	5939.05	0.0000	0.0016
6225.85–6331.78	18	6268.04	0.0004	0.0015
6596.84–6718.78	14	6642.96	-0.0044	0.0012
6963.84–7076.77	22	7016.17	-0.0029	0.0027
7383.81–7438.77	10	7417.98	-0.0009	0.0024
7727.83–7793.78	17	7775.85	-0.0029	0.0023
8100.82–8174.77	20	8137.40	-0.0008	0.0016
8517.78–8525.79	6	8522.78	0.0002	0.0014
8792.84–8874.79	12	8831.32	-0.0017	0.0015
9102.00–9291.60	64	9178.87	-0.0004	0.0019
9471.00–9689.60	68	9571.66	0.0001	0.0017
9814.00–10054.60	58	9917.75	0.0009	0.0013
10204.00–10266.00	24	10222.96	0.0023	0.0016
10614.90–10781.60	36	10690.41	0.0004	0.0018
10893.00–11123.60	36	11047.45	0.0020	0.0017
11275.00–11496.60	33	11441.12	0.0003	0.0013
11629.00–11867.60	24	11750.03	-0.0010	0.0016
12037.90–12067.90	6	12060.57	0.0016	0.0011
12413.00–12590.60	39	12489.92	0.0001	0.0019
12741.00–12815.90	13	12788.49	0.0019	0.0018

Table A.27. HD 190007 photometric observing seasons (in JD-2440000).

JD range	N _{obs}	JD _{mean}	$\Delta(b + y)/2_{\text{mean}}$	σ_{by}
5862.86–6015.77	36	5958.41	0.0027	0.0076
6219.86–6376.77	37	6270.12	-0.0005	0.0038
6588.85–6732.77	48	6641.82	-0.0074	0.0059
6957.85–7086.77	58	7021.71	0.0029	0.0083
7349.84–7456.77	40	7415.05	0.0044	0.0045
7741.82–7793.79	36	7772.75	0.0074	0.0036
8094.83–8190.77	40	8138.60	0.0010	0.0039
8474.82–8537.78	16	8518.92	0.0075	0.0046
8824.83–8892.80	20	8859.01	0.0027	0.0042
9095.00–9318.60	59	9192.31	0.0042	0.0040
9466.00–9662.60	62	9567.10	-0.0078	0.0092
9832.00–10040.60	63	9951.08	0.0013	0.0055
10198.00–10366.77	42	10282.24	-0.0104	0.0101
10563.00–10768.60	42	10692.74	-0.0010	0.0038
10937.00–11134.60	42	11056.81	0.0020	0.0050
11296.00–11354.90	8	11327.19	0.0040	0.0021
11448.79–11499.60	24	11462.16	0.0032	0.0022
11678.90–11710.90	9	11694.27	0.0030	0.0035
12061.90–12077.00	8	12068.94	-0.0058	0.0028
12214.60–12228.60	5	12220.00	0.0012	0.0008
12392.00–12461.90	19	12426.67	-0.0032	0.0048
12537.70–12600.60	20	12560.46	0.0008	0.0029
12748.00–12812.90	16	12784.92	-0.0027	0.0026

Table A.28. HD 201091 photometric observing seasons (in JD-2440000).

JD range	N _{obs}	JD _{mean}	$\Delta(b + y)/2_{\text{mean}}$	σ_{by}
5862.86–6015.77	38	5958.62	0.0023	0.0026
6234.85–6376.77	34	6302.88	0.0041	0.0020
6590.85–6728.78	28	6658.64	-0.0008	0.0018
6965.84–7086.79	39	7039.35	0.0001	0.0027
7349.84–7456.78	38	7411.18	0.0023	0.0026
7722.84–7792.80	34	7767.81	0.0010	0.0021
8094.84–8202.79	38	8134.95	-0.0003	0.0017
8438.84–8464.84	3	8447.51	0.0005	0.0000
8792.84–8888.81	28	8849.54	-0.0019	0.0017
9178.84–9255.80	12	9213.32	-0.0022	0.0031
9528.84–9611.79	27	9564.46	-0.0006	0.0036
9922.83–10003.78	24	9976.88	0.0013	0.0024
10301.83–10441.60	39	10363.30	0.0011	0.0017
10613.90–10800.60	48	10720.87	-0.0003	0.0024
10914.00–11172.60	40	11085.72	-0.0053	0.0025
11449.80–11535.60	27	11482.61	-0.0017	0.0018
11807.90–11908.60	16	11869.75	-0.0003	0.0016
12228.70–12275.60	9	12263.17	-0.0010	0.0024
12369.00–12448.90	28	12430.55	0.0002	0.0011
12537.80–12634.60	45	12583.88	0.0000	0.0024
12733.00–12816.00	28	12792.65	0.0002	0.0028

Table A.29. HD 201092 photometric observing seasons (in JD-2440000).

JD range	N _{obs}	JD _{mean}	$\Delta(b+y)/2_{\text{mean}}$	σ_{by}
5862.86–6015.77	39	5958.45	0.0020	0.0022
6234.85–6376.77	33	6302.48	0.0036	0.0020
6590.85–6728.78	28	6658.64	0.0032	0.0016
6965.84–7086.79	39	7039.35	0.0021	0.0016
7349.84–7456.78	38	7411.18	0.0037	0.0026
7722.84–7792.80	34	7767.81	-0.0002	0.0027
8094.84–8202.79	38	8134.95	-0.0023	0.0020
8438.84–8464.84	4	8451.84	-0.0021	0.0017
8792.84–8888.81	28	8849.54	-0.0021	0.0025
9178.84–9255.80	12	9213.32	-0.0046	0.0024
9528.84–9611.79	27	9564.46	-0.0024	0.0025
9922.83–10003.78	24	9976.88	-0.0025	0.0018
10301.83–10373.77	28	10341.73	-0.0030	0.0021
10712.80–10754.77	20	10726.50	-0.0015	0.0019
11045.81–11094.79	14	11079.94	-0.0041	0.0024
11449.80–11500.77	19	11477.63	0.0007	0.0019

Table A.30. HD 206860 photometric observing seasons (in JD-2440000).

JD range	N _{obs}	JD _{mean}	V _{mean}	σ_V
7901.57–7901.75	3	7901.66	5.9817	0.0040
8017.71–8066.95	9	8056.78	5.9810	0.0105
8202.57–8249.68	8	8231.97	5.9822	0.0046
8363.59–8412.84	12	8382.81	5.9782	0.0068
8550.01–8565.75	8	8557.88	5.9654	0.0046
8758.04–8806.57	16	8783.24	5.9782	0.0109
9126.97–9163.92	22	9147.16	5.9724	0.0062
9239.73–9337.57	43	9272.48	5.9729	0.0058
9491.97–9547.95	18	9525.71	5.9769	0.0044
9633.70–9706.57	36	9663.89	5.9753	0.0066
9862.96–9908.84	33	9881.87	5.9786	0.0101
9986.70–10071.57	33	10022.10	5.9804	0.0112
10392.71–10443.58	20	10422.48	5.9752	0.0116
10620.97–10642.95	3	10628.96	5.9820	0.0026
10714.82–10806.59	33	10755.31	5.9725	0.0075
11010.53–11024.48	12	11015.37	5.9701	0.0136
11077.74–11179.57	51	11124.51	5.9731	0.0066

Table B.1. HD 1835 S-index observing seasons (in JD-2440000).

JD range	N _{obs}	JD _{mean}	S _{mean}	σ_S
4423.93–4608.60	244	4487.05	0.3457	0.0126
4803.99–4920.69	177	4869.14	0.3319	0.0155
5198.93–5309.63	68	5236.36	0.3423	0.0182
5542.98–5725.61	130	5632.87	0.3475	0.0170
5905.97–6069.64	160	5983.71	0.3408	0.0180
6283.96–6427.70	139	6353.10	0.3257	0.0122
6654.99–6808.61	165	6710.21	0.3313	0.0126
7027.91–7183.60	159	7089.48	0.3161	0.0132
7388.95–7541.60	161	7453.66	0.3002	0.0116
7766.92–7878.67	75	7826.33	0.3341	0.0180
8108.98–8244.62	75	8183.79	0.3367	0.0148
8489.97–8649.60	45	8602.55	0.3643	0.0138
8869.91–8988.64	117	8918.89	0.3636	0.0179
9227.95–9344.62	94	9287.36	0.3515	0.0270
9581.90–9736.61	183	9647.64	0.3444	0.0176
9951.93–10096.62	108	10013.95	0.3534	0.0144
10311.99–10458.61	117	10376.43	0.3586	0.0182
10676.95–10809.62	72	10719.09	0.3473	0.0139
11047.93–11186.62	102	11120.61	0.3869	0.0160
11406.91–11557.60	86	11487.55	0.3744	0.0196
11778.89–11900.64	33	11841.12	0.3693	0.0186
12121.94–12197.79	42	12163.00	0.3655	0.0203

Table B.2. HD 10476 S-index observing seasons (in JD-2440000).

JD range	N _{obs}	JD _{mean}	S _{mean}	σ_S
3347.80–3481.80	9	3414.80	0.2067	0.0098
3742.80–3892.80	7	3795.23	0.1963	0.0018
4172.80–4226.80	5	4203.40	0.1841	0.0035
4412.00–4566.76	190	4477.34	0.1770	0.0046
4828.01–4900.91	30	4866.93	0.1731	0.0045
5197.97–5345.67	107	5252.16	0.1765	0.0047
5544.97–5743.62	138	5658.10	0.1969	0.0071
5883.99–6070.69	54	5961.79	0.2165	0.0102
6286.00–6470.63	114	6383.20	0.2093	0.0082
6672.99–6817.62	93	6731.20	0.2108	0.0099
7024.93–7198.65	111	7098.47	0.1942	0.0059
7406.00–7559.62	78	7484.01	0.1788	0.0044
7766.00–7912.61	75	7832.82	0.1824	0.0102
8122.98–8256.66	57	8181.18	0.1734	0.0047
8597.70–8677.63	42	8635.03	0.1750	0.0047
8873.88–9015.62	78	8936.08	0.1742	0.0042
9251.93–9368.63	99	9310.46	0.1777	0.0032
9581.94–9755.62	132	9660.45	0.1846	0.0056
9957.00–10107.61	87	10032.03	0.1878	0.0077
10315.95–10482.61	101	10395.07	0.2005	0.0096
10700.92–10841.61	53	10755.48	0.1875	0.0052
11073.92–11211.60	78	11140.87	0.1878	0.0085
11457.92–11557.66	51	11513.83	0.1829	0.0081
11779.94–11907.62	33	11855.31	0.1740	0.0072
12141.99–12190.86	24	12163.53	0.1691	0.0059

Table B.3. HD 13421 S-index observing seasons (in JD-2440000).

JD range	N _{obs}	JD _{mean}	S _{mean}	σ_S
4423.97–4566.79	184	4479.53	0.1287	0.0029
4828.00–4986.65	52	4906.68	0.1305	0.0034
5193.00–5375.60	159	5280.31	0.1285	0.0040
5544.98–5743.64	194	5653.71	0.1283	0.0042
5918.96–6119.65	271	6009.33	0.1288	0.0045
6291.98–6472.63	243	6392.43	0.1285	0.0030
6673.94–6845.61	244	6751.18	0.1281	0.0038
7024.97–7213.61	332	7118.74	0.1296	0.0034
7416.94–7579.61	258	7489.30	0.1288	0.0042
7762.01–7942.61	282	7856.87	0.1292	0.0030
8109.01–8301.61	199	8217.11	0.1310	0.0032
8576.80–8657.62	63	8631.66	0.1321	0.0035
8873.89–9020.62	185	8942.78	0.1291	0.0029
9250.92–9375.62	185	9313.10	0.1275	0.0025
9600.93–9769.61	235	9685.95	0.1271	0.0035
9951.99–10127.60	178	10034.67	0.1275	0.0033
10315.00–10485.61	189	10395.99	0.1285	0.0037
10704.93–10844.61	93	10763.09	0.1297	0.0043
11067.93–11213.62	165	11141.12	0.1302	0.0046
11441.91–11571.61	131	11512.28	0.1291	0.0039
11779.95–11913.64	79	11851.57	0.1288	0.0041
12138.96–12205.83	63	12165.73	0.1249	0.0045

Table B.4. HD 18256 S-index observing seasons (in JD-2440000).

JD range	N _{obs}	JD _{mean}	S _{mean}	σ_S
4849.99–5026.64	24	4888.04	0.1819	0.0040
5211.97–5346.64	54	5264.49	0.1755	0.0045
5569.02–5741.65	123	5670.71	0.1798	0.0056
5918.94–6121.63	134	6011.01	0.1906	0.0061
6304.00–6486.62	219	6398.11	0.1886	0.0041
6673.99–6831.65	168	6740.01	0.1790	0.0048
7025.00–7215.61	209	7118.95	0.1798	0.0052
7420.97–7564.64	126	7484.25	0.1749	0.0048
7803.99–7942.62	75	7870.86	0.1759	0.0038
8152.99–8300.64	69	8233.79	0.1808	0.0053
8645.65–8657.60	14	8652.63	0.1697	0.0034
8886.00–9019.66	120	8948.63	0.1823	0.0040
9264.97–9369.66	39	9317.41	0.1837	0.0054
9615.89–9766.61	37	9680.20	0.1764	0.0044
9978.97–10127.61	36	10038.65	0.1690	0.0044
10316.95–10482.65	45	10402.28	0.1642	0.0035
10709.94–10844.64	33	10771.54	0.1640	0.0057
11070.96–11212.66	36	11144.71	0.1851	0.0064
11442.92–11572.61	36	11510.28	0.1667	0.0043
11803.96–11913.66	15	11879.35	0.2012	0.0254
12146.00–12181.89	12	12162.19	0.1790	0.0056

Table B.5. HD 20630 S-index observing seasons (in JD-2440000).

JD range	N _{obs}	JD _{mean}	S _{mean}	σ_S
4172.80–4260.80	12	4207.38	0.3661	0.0128
4426.98–4659.64	253	4511.54	0.3519	0.0112
4848.00–4900.96	102	4872.72	0.3362	0.0105
5199.01–5375.61	69	5260.97	0.3362	0.0083
5563.99–5756.61	63	5700.05	0.3514	0.0125
5918.98–6125.61	177	6022.36	0.3561	0.0133
6301.97–6487.67	177	6388.84	0.3416	0.0108
6678.97–6843.64	148	6743.18	0.3402	0.0125
7024.99–7216.63	189	7108.04	0.3290	0.0139
7420.98–7574.65	135	7484.70	0.3454	0.0095
7804.02–7942.63	79	7861.40	0.3698	0.0114
8166.00–8311.62	84	8248.89	0.3641	0.0144
8597.75–8694.63	66	8642.69	0.3555	0.0141
8873.91–9051.64	105	8946.18	0.3370	0.0142
9265.92–9399.65	84	9330.95	0.3273	0.0123
9615.91–9771.62	126	9691.19	0.3309	0.0156

Table B.6. HD 25998 S-index observing seasons (in JD-2440000).

JD range	N _{obs}	JD _{mean}	S _{mean}	σ_S
4446.99–4658.66	235	4514.18	0.2903	0.0084
4869.03–4886.91	15	4877.14	0.2877	0.0068
5212.00–5349.69	29	5268.76	0.2805	0.0083
5576.03–5772.65	126	5680.79	0.2771	0.0089
5945.01–6121.65	102	6028.96	0.2858	0.0092
6329.98–6496.63	174	6412.01	0.2826	0.0066
6703.03–6845.68	116	6757.27	0.2825	0.0076
7047.01–7240.64	157	7151.76	0.2746	0.0069
7444.84–7574.68	123	7500.30	0.2685	0.0060
7805.00–7942.66	63	7867.74	0.2735	0.0058
8121.98–8312.66	75	8256.29	0.2755	0.0075
8639.68–8696.64	45	8662.27	0.2744	0.0058
8908.90–9019.69	87	8959.05	0.2570	0.0057
9300.84–9397.67	18	9341.59	0.2705	0.0056
9642.92–9759.68	27	9697.92	0.2746	0.0053
9983.00–10137.62	30	10050.24	0.2784	0.0132
10342.95–10500.62	30	10411.43	0.2658	0.0070
10766.89–10844.66	18	10810.41	0.2629	0.0075
11067.98–11222.66	27	11145.61	0.2632	0.0077
11441.98–11571.67	15	11499.85	0.2538	0.0076
11805.01–11943.63	24	11884.92	0.2632	0.0151
12153.00–12205.89	9	12176.28	0.2673	0.0118

Table B.7. HD 35296 S-index observing seasons (in JD-2440000).

JD range	N _{obs}	JD _{mean}	S _{mean}	σ_S
4545.96–4681.64	69	4609.95	0.3147	0.0085
4871.03–5026.70	33	4913.23	0.3182	0.0074
5247.97–5432.65	96	5335.69	0.3105	0.0092
5591.03–5794.69	203	5727.50	0.3096	0.0102
5958.99–6122.70	105	6045.11	0.3082	0.0088
6330.01–6516.67	207	6427.72	0.3165	0.0089
6713.03–6877.63	141	6777.85	0.3117	0.0082
7058.02–7242.67	156	7158.63	0.3007	0.0076
7450.98–7592.67	105	7515.54	0.2933	0.0072
7832.99–7957.68	87	7889.91	0.2938	0.0068
8135.99–8346.63	78	8271.90	0.2948	0.0075
8576.91–8722.63	69	8668.41	0.2869	0.0081
8929.00–9069.64	81	9000.97	0.2845	0.0114
9296.95–9433.66	121	9359.44	0.2920	0.0070
9647.92–9784.67	156	9715.56	0.2894	0.0101
10011.99–10160.65	114	10089.97	0.2922	0.0115
10345.97–10522.65	132	10445.48	0.2850	0.0093
10761.93–10884.66	96	10826.98	0.2846	0.0131
11106.93–11250.64	121	11169.40	0.3019	0.0121
11471.96–11623.63	111	11531.38	0.2866	0.0119
11837.94–11940.70	48	11897.94	0.2982	0.0159

Table B.8. HD 39587 S-index observing seasons (in JD-2440000).

JD range	N _{obs}	JD _{mean}	S _{mean}	σ_S
4545.97–4681.65	72	4610.79	0.3101	0.0089
4874.98–5026.69	66	4947.15	0.3165	0.0115
5248.00–5431.66	90	5332.46	0.3203	0.0103
5592.02–5802.66	840	5702.05	0.3085	0.0055
5978.01–6156.67	141	6051.21	0.3162	0.0105
6330.01–6525.63	893	6448.73	0.3183	0.0068
6713.02–6877.64	132	6779.05	0.3125	0.0131
7065.01–7263.69	201	7152.61	0.3131	0.0118
7421.03–7621.64	153	7511.13	0.3007	0.0094
7826.96–7957.69	81	7877.63	0.3018	0.0077
8209.96–8347.64	90	8265.18	0.2978	0.0085
8597.85–8732.65	102	8664.44	0.3087	0.0066
8874.93–9069.64	84	8977.03	0.2989	0.0119
9299.95–9433.67	111	9356.35	0.2927	0.0098
9660.94–9784.68	138	9716.19	0.2936	0.0084
10012.00–10160.66	104	10097.80	0.2860	0.0174
10347.00–10537.62	151	10467.07	0.3022	0.0110
10761.98–10884.67	90	10825.55	0.2892	0.0103
11117.97–11257.62	114	11186.37	0.3251	0.0154
11471.98–11623.63	105	11536.90	0.3183	0.0134
11862.89–11988.62	48	11910.68	0.3209	0.0170

Table B.9. HD 72905 S-index observing seasons (in JD-2440000).

JD range	N _{obs}	JD _{mean}	S _{mean}	σ_S
5634.06–5812.69	114	5739.52	0.3524	0.0102
6004.00–6189.69	90	6129.99	0.3583	0.0118
6375.03–6553.71	116	6472.71	0.3644	0.0103
6740.02–6906.64	93	6830.12	0.3577	0.0127
7107.99–7295.71	118	7199.89	0.3584	0.0126
7467.02–7631.66	90	7560.80	0.3544	0.0162
7863.00–7975.76	26	7898.64	0.3671	0.0093
8167.99–8361.68	36	8283.42	0.3855	0.0188
8656.81–8732.69	12	8709.71	0.3693	0.0136
9015.91–9102.67	27	9079.39	0.3500	0.0095
9326.96–9464.67	46	9406.74	0.3659	0.0128
9759.85–9793.74	9	9775.13	0.3781	0.0061

Table B.10. HD 75332 S-index observing seasons (in JD-2440000).

JD range	N _{obs}	JD _{mean}	S _{mean}	σ_S
3236.80–3238.80	3	3237.80	0.2845	0.0077
3476.80–3542.80	4	3494.05	0.2688	0.0208
3891.80–3984.80	4	3917.05	0.2761	0.0031
4169.80–4277.80	15	4215.20	0.2771	0.0054
4545.97–4710.65	90	4651.94	0.2511	0.0082
4875.00–5082.67	39	5014.33	0.2517	0.0091
5308.97–5440.64	120	5373.58	0.2720	0.0084
5634.02–5853.68	309	5758.25	0.2735	0.0090
6010.02–6193.72	180	6141.00	0.2776	0.0090
6383.03–6553.75	227	6477.82	0.2724	0.0074
6748.04–6921.66	157	6842.01	0.2928	0.0111
7110.01–7297.66	226	7195.71	0.2825	0.0070
7472.02–7631.67	138	7566.47	0.2720	0.0086
7832.04–7981.72	99	7907.84	0.2800	0.0106
8186.97–8375.66	123	8293.28	0.2976	0.0094
8646.78–8741.66	72	8695.46	0.2843	0.0082
8977.00–9118.66	125	9056.03	0.2736	0.0085
9313.01–9463.72	24	9388.10	0.2798	0.0079
9688.98–9795.76	18	9740.05	0.2777	0.0065
10085.99–10179.69	18	10132.98	0.2737	0.0083
10434.93–10564.67	24	10495.44	0.2861	0.0102
10805.99–10932.64	21	10870.67	0.2749	0.0091
11165.96–11304.65	63	11257.08	0.2946	0.0126
11525.94–11646.70	72	11592.43	0.2837	0.0122
11898.96–12001.67	42	11942.68	0.2813	0.0112

Table B.11. HD 81809 S-index observing seasons (in JD-2440000).

JD range	N _{obs}	JD _{mean}	S _{mean}	σ_S
3236.80–3257.80	5	3245.60	0.1778	0.0072
3891.80–3984.80	5	3930.40	0.1698	0.0033
4191.80–4277.80	6	4235.97	0.1612	0.0049
4546.02–4710.68	105	4654.37	0.1628	0.0058
4940.02–5082.69	36	5009.36	0.1783	0.0044
5298.04–5440.69	138	5366.08	0.1817	0.0075
5634.04–5813.73	60	5729.59	0.1841	0.0064
6071.02–6189.66	78	6141.55	0.1780	0.0042
6410.05–6570.67	120	6489.82	0.1722	0.0042
6767.07–6922.66	86	6843.56	0.1669	0.0061
7125.05–7306.67	99	7212.95	0.1626	0.0047
7495.99–7639.69	76	7569.84	0.1613	0.0051
7866.03–7981.74	39	7923.90	0.1684	0.0065
8243.99–8375.68	48	8304.11	0.1803	0.0052
8598.02–8760.67	108	8678.56	0.1809	0.0051
9011.96–9106.67	24	9073.02	0.1775	0.0044
9335.96–9486.67	141	9411.89	0.1709	0.0046
9705.00–9819.74	81	9760.91	0.1629	0.0050
10084.98–10207.68	102	10145.65	0.1614	0.0051
10434.98–10570.66	114	10504.72	0.1675	0.0082
10814.94–10934.66	66	10888.41	0.1660	0.0055
11161.97–11305.66	87	11243.93	0.1766	0.0065
11525.96–11660.65	72	11595.98	0.1795	0.0064
11891.98–11996.72	42	11939.36	0.1850	0.0088

Table B.12. HD 82443 S-index observing seasons (in JD-2440000).

JD range	N _{obs}	JD _{mean}	S _{mean}	σ_S
6558.69–6575.67	21	6566.82	0.5911	0.0256
6768.05–6921.68	111	6848.00	0.6372	0.0394
7133.05–7308.66	205	7218.38	0.5939	0.0222
7496.02–7648.69	123	7573.08	0.5799	0.0294
7863.04–7981.76	84	7911.85	0.6939	0.0308
8240.99–8376.71	72	8303.00	0.6599	0.0221
8651.92–8771.70	75	8720.71	0.6850	0.0291
8991.98–9130.67	93	9076.42	0.6593	0.0210
9335.97–9487.67	160	9413.54	0.6423	0.0279
9714.00–9819.76	84	9770.78	0.7078	0.0571

Table B.13. HD 82885 S-index observing seasons (in JD-2440000).

JD range	N _{obs}	JD _{mean}	S _{mean}	σ_S
4546.03–4775.67	199	4702.87	0.2825	0.0207
4875.02–5121.69	155	5018.97	0.2776	0.0135
5298.04–5440.65	150	5363.79	0.2877	0.0111
5634.03–5853.70	123	5755.63	0.2847	0.0125
6010.04–6211.72	87	6146.29	0.2981	0.0155
6417.96–6577.67	141	6498.35	0.2942	0.0135
6768.06–6934.67	96	6854.33	0.2720	0.0134
7142.05–7307.69	108	7221.67	0.2596	0.0138
7496.04–7648.70	84	7572.12	0.2451	0.0108
7866.04–7981.76	51	7924.25	0.2446	0.0088
8193.04–8375.70	51	8296.42	0.2351	0.0082
8598.06–8771.70	111	8686.65	0.2797	0.0130
8992.00–9126.69	60	9080.38	0.2438	0.0075
9359.94–9485.69	59	9429.23	0.2767	0.0171
9753.90–9818.77	27	9783.72	0.2682	0.0119
10090.94–10219.67	89	10155.17	0.2606	0.0133
10434.99–10570.67	96	10504.54	0.2619	0.0103
10814.96–10934.67	57	10886.00	0.2642	0.0152
11197.91–11308.67	69	11255.40	0.2376	0.0115
11527.96–11682.66	66	11620.71	0.2628	0.0168
11891.96–12025.64	42	11948.48	0.2770	0.0097

Table B.14. HD 103095 S-index observing seasons (in JD-2440000).

JD range	N _{obs}	JD _{mean}	S _{mean}	σ_S
3236.80–3257.80	5	3242.20	0.2059	0.0050
3478.80–3631.80	4	3571.05	0.2068	0.0169
3891.80–4005.80	6	3967.30	0.1928	0.0030
4224.80–4277.80	3	4254.47	0.1837	0.0055
4565.02–4775.72	177	4709.06	0.1739	0.0056
4992.97–5140.69	144	5065.55	0.1750	0.0089
5346.98–5449.76	92	5401.15	0.1861	0.0050
5671.07–5874.70	60	5788.60	0.1902	0.0049
6085.74–6244.69	84	6175.63	0.1983	0.0059
6443.96–6605.70	139	6532.64	0.1911	0.0052
6807.06–6951.70	56	6882.70	0.1818	0.0066
7168.00–7347.71	116	7252.24	0.1727	0.0039
7509.03–7666.70	69	7604.38	0.1702	0.0042
7926.00–7977.89	27	7945.96	0.1892	0.0036
8282.02–8408.70	33	8378.77	0.1936	0.0039
8655.92–8797.70	69	8757.67	0.1929	0.0045
9067.88–9136.69	15	9105.18	0.1921	0.0028
9360.97–9528.69	90	9472.24	0.1821	0.0059
9753.95–9881.68	21	9821.66	0.1779	0.0052
10108.96–10243.68	72	10187.10	0.1805	0.0053
10466.00–10602.68	93	10541.35	0.1852	0.0061
10837.96–10966.71	51	10901.13	0.1919	0.0076
11197.96–11327.70	76	11265.76	0.2046	0.0070
11556.99–11701.68	73	11636.68	0.1967	0.0070
11932.94–12055.67	41	11997.26	0.1881	0.0080

Table B.15. HD 115383 S-index observing seasons (in JD-2440000).

JD range	N _{obs}	JD _{mean}	S _{mean}	σ_S
3235.80–3297.80	11	3262.62	0.2947	0.0108
3631.80–3676.80	4	3659.30	0.2995	0.0051
3891.80–4051.80	15	3982.40	0.3103	0.0241
4641.02–4779.71	138	4730.85	0.3213	0.0087
4992.99–5151.69	192	5087.58	0.3032	0.0088
5345.93–5485.71	162	5414.28	0.3109	0.0085
5699.08–5922.66	102	5829.94	0.3164	0.0095
6098.06–6184.88	19	6121.73	0.3025	0.0091
6457.99–6615.73	54	6528.21	0.2892	0.0056
6828.01–6963.73	48	6895.27	0.2998	0.0092
7186.05–7336.71	81	7275.14	0.3085	0.0084
7544.01–7666.75	48	7608.96	0.2827	0.0078
7929.03–8074.69	18	7971.93	0.2835	0.0047
8253.03–8431.71	102	8361.71	0.2907	0.0065
8655.96–8794.72	111	8748.54	0.2960	0.0061
9048.93–9153.71	42	9097.83	0.2814	0.0071
9421.91–9548.71	27	9482.79	0.2832	0.0065
9764.98–9881.73	12	9809.87	0.2762	0.0038
10105.99–10270.67	33	10185.57	0.2860	0.0082
10467.98–10622.68	27	10553.04	0.2815	0.0130
10860.98–10986.68	27	10920.51	0.2864	0.0111
11235.95–11314.77	18	11276.01	0.2887	0.0080
11567.00–11728.67	31	11645.96	0.2918	0.0087
11933.00–12061.68	21	11995.57	0.2976	0.0099

Table B.16. HD 115404 S-index observing seasons (in JD-2440000).

JD range	N _{obs}	JD _{mean}	S _{mean}	σ_S
4657.95–4808.69	224	4751.60	0.5741	0.0315
4987.02–5151.69	216	5086.07	0.5388	0.0271
5344.06–5485.70	153	5415.65	0.5445	0.0248
5706.07–5919.68	126	5829.23	0.5245	0.0280
6085.89–6250.68	127	6182.48	0.5195	0.0196
6458.99–6627.68	150	6552.49	0.4984	0.0289
6832.06–6965.71	78	6911.39	0.4904	0.0289
7186.01–7350.72	132	7274.45	0.4707	0.0227
7544.02–7686.70	84	7619.57	0.4579	0.0311
7918.05–8075.69	33	7974.74	0.5273	0.0339
8253.02–8432.72	39	8372.45	0.5162	0.0230
8656.97–8822.71	81	8762.34	0.4950	0.0172
9048.94–9159.73	75	9100.28	0.5143	0.0342
9406.99–9547.70	117	9481.31	0.5168	0.0255
9764.99–9882.71	39	9825.46	0.4926	0.0185
10144.96–10270.68	78	10205.66	0.4942	0.0385
10500.97–10631.69	99	10560.65	0.4564	0.0269
10887.94–10987.68	57	10936.02	0.4684	0.0205
11235.95–11340.75	66	11281.43	0.4976	0.0218
11570.96–11727.68	82	11658.21	0.4879	0.0314
11945.00–12054.73	30	12010.12	0.5200	0.0357

Table B.17. HD 120136 S-index observing seasons (in JD-2440000).

JD range	N _{obs}	JD _{mean}	S _{mean}	σ_S
4987.03–5164.66	207	5110.21	0.1859	0.0035
5345.94–5505.68	189	5431.82	0.1882	0.0057
5705.04–5922.69	411	5811.28	0.1903	0.0053
6089.26–6250.69	250	6188.53	0.1855	0.0054
6453.94–6631.66	498	6507.38	0.1832	0.0045
6831.07–7006.67	138	6919.01	0.1860	0.0047
7186.02–7357.67	189	7278.88	0.1894	0.0044
7545.02–7738.70	97	7626.67	0.1886	0.0043
7933.04–8071.72	18	7982.92	0.1884	0.0023
8256.01–8431.72	40	8380.41	0.1900	0.0038
8655.01–8822.71	153	8750.79	0.1883	0.0035
9057.91–9163.74	105	9112.74	0.1851	0.0038
9420.95–9548.72	234	9491.75	0.1917	0.0042
9769.00–9917.69	66	9854.43	0.1933	0.0052
10110.00–10273.68	174	10206.17	0.1860	0.0059
10468.01–10643.68	273	10570.19	0.1870	0.0052
10863.96–11004.68	149	10936.78	0.1873	0.0063
11235.98–11357.66	102	11290.45	0.1957	0.0085
11593.98–11728.69	141	11666.83	0.1896	0.0067
11943.03–12081.67	87	12020.23	0.1947	0.0085

Table B.18. HD 124570 S-index observing seasons (in JD-2440000).

JD range	N _{obs}	JD _{mean}	S _{mean}	σ_S
4671.94–4810.67	129	4740.89	0.1316	0.0034
4993.02–5173.66	268	5104.40	0.1322	0.0037
5345.96–5553.67	246	5451.92	0.1322	0.0035
5708.05–5939.64	315	5826.91	0.1334	0.0051
6083.51–6294.65	349	6189.80	0.1335	0.0035
6457.02–6631.67	319	6557.31	0.1330	0.0041
6855.06–7036.67	261	6936.44	0.1348	0.0047
7191.07–7383.66	428	7283.16	0.1346	0.0042
7573.96–7740.66	228	7652.73	0.1328	0.0038
7917.08–8098.67	102	8040.48	0.1339	0.0028
8290.05–8466.68	237	8400.73	0.1325	0.0027
8655.98–8831.68	213	8759.23	0.1339	0.0029
9048.96–9195.70	182	9124.32	0.1322	0.0036
9407.00–9560.68	285	9495.79	0.1320	0.0025
9792.94–9932.68	170	9876.06	0.1302	0.0029
10110.01–10274.69	174	10214.43	0.1312	0.0041
10500.99–10643.69	215	10578.45	0.1317	0.0037
10872.01–11004.69	127	10948.96	0.1320	0.0040
11235.99–11357.67	108	11291.00	0.1320	0.0042
11594.00–11728.71	169	11672.54	0.1333	0.0042
11933.01–12089.67	99	12025.78	0.1340	0.0045

Table B.19. HD 129333 S-index observing seasons (in JD-2440000).

JD range	N _{obs}	JD _{mean}	S _{mean}	σ_S
5489.76–5553.68	56	5509.35	0.5353	0.0238
5705.05–5893.71	255	5819.97	0.5249	0.0245
6111.03–6289.67	141	6200.89	0.5125	0.0228
6472.99–6639.74	167	6576.34	0.5257	0.0192
6855.01–7001.72	90	6928.16	0.5540	0.0287
7204.04–7378.70	192	7301.88	0.5423	0.0235
7577.91–7728.68	107	7650.32	0.5299	0.0459
7974.95–8088.69	15	8018.86	0.6014	0.0212
8345.98–8461.70	60	8414.38	0.5916	0.0273
8722.88–8822.73	84	8782.60	0.5822	0.0270
9067.98–9186.72	86	9131.35	0.5906	0.0347
9434.92–9558.70	128	9506.04	0.5774	0.0246
9927.69–9932.68	15	9930.29	0.5759	0.0235
10180.92–10273.68	96	10229.11	0.5660	0.0760

Table B.20. HD 131156A S-index observing seasons (in JD-2440000).

JD range	N _{obs}	JD _{mean}	S _{mean}	σ_S
4656.02–4810.68	249	4746.31	0.4547	0.0164
4996.03–5184.66	345	5110.90	0.4576	0.0160
5345.99–5523.70	171	5436.90	0.4309	0.0213
5710.08–5951.63	645	5834.01	0.4701	0.0236
6097.71–6287.68	276	6195.53	0.4610	0.0161
6419.05–6689.63	305	6569.75	0.4368	0.0184
6857.01–7034.68	129	6937.45	0.4200	0.0170
7204.05–7384.70	215	7305.67	0.4478	0.0146
7546.01–7727.68	132	7643.43	0.4241	0.0270
7918.08–8090.68	39	7983.55	0.4698	0.0130
8274.99–8466.69	141	8381.11	0.4479	0.0125
8671.98–8831.69	177	8760.15	0.4570	0.0146
9048.97–9209.66	150	9135.72	0.4436	0.0199
9407.01–9570.67	248	9496.85	0.4712	0.0130
9802.97–9933.67	75	9888.93	0.4953	0.0183
10136.98–10284.67	153	10224.21	0.4716	0.0330
10501.01–10662.66	199	10584.02	0.4102	0.0123
10896.94–11025.67	93	10954.75	0.4189	0.0130
11249.98–11378.66	96	11303.80	0.4449	0.0165
11605.97–11735.71	134	11681.62	0.4083	0.0188
11982.96–12089.69	81	12036.96	0.4035	0.0226

Table B.21. HD 143761 S-index observing seasons (in JD-2440000).

JD range	N _{obs}	JD _{mean}	S _{mean}	σ_S
4673.97–4795.73	132	4743.22	0.1509	0.0043
5027.05–5198.67	174	5136.44	0.1494	0.0038
5346.03–5560.67	258	5481.91	0.1501	0.0037
5729.06–5964.64	243	5883.55	0.1503	0.0057
6108.05–6304.69	249	6226.05	0.1505	0.0029
6486.03–6676.64	237	6589.81	0.1492	0.0036
6858.00–7067.65	205	6970.32	0.1491	0.0044
7226.95–7422.62	327	7335.72	0.1479	0.0032
7575.00–7760.70	228	7688.90	0.1493	0.0031
7950.98–8134.65	144	8099.47	0.1491	0.0025
8286.02–8467.71	129	8410.82	0.1493	0.0023
8693.99–8890.63	297	8813.60	0.1500	0.0026
9097.96–9225.67	191	9174.20	0.1504	0.0040
9434.95–9559.73	224	9504.08	0.1495	0.0025
9854.85–9961.66	156	9919.64	0.1485	0.0027
10174.00–10305.68	186	10250.11	0.1505	0.0047
10525.93–10676.65	222	10608.64	0.1489	0.0035
10919.93–11032.68	116	10978.65	0.1480	0.0041
11254.97–11400.66	146	11326.99	0.1483	0.0042
11606.01–11755.66	154	11686.03	0.1478	0.0042
11986.94–12115.66	96	12045.39	0.1475	0.0049

Table B.22. HD 149661 S-index observing seasons (in JD-2440000).

JD range	N _{obs}	JD _{mean}	S _{mean}	σ_S
4465.69–4528.61	127	4495.36	0.3394	0.0240
4656.04–4875.63	285	4760.74	0.3312	0.0143
4996.05–5212.65	319	5124.66	0.3024	0.0149
5367.09–5557.69	231	5480.26	0.3064	0.0184
5728.09–5965.68	395	5852.24	0.3254	0.0187
6139.05–6329.62	316	6245.06	0.3266	0.0178
6514.99–6687.64	222	6601.61	0.3019	0.0184
6890.99–7057.67	162	6971.62	0.3570	0.0160
7242.03–7421.62	210	7338.41	0.3714	0.0184
7575.99–7758.67	102	7676.86	0.3471	0.0215
8068.78–8123.67	36	8099.72	0.3396	0.0141
8361.98–8466.72	84	8422.97	0.3380	0.0149
8677.97–8882.65	231	8799.96	0.3010	0.0097
9049.00–9249.63	144	9192.21	0.3119	0.0166
9445.00–9597.66	252	9529.17	0.3171	0.0127
9854.90–9970.63	108	9931.23	0.3313	0.0162
10195.96–10329.64	144	10270.04	0.3519	0.0212
10525.97–10703.63	201	10616.89	0.3255	0.0152
10921.99–11052.65	96	10981.82	0.2984	0.0193
11254.98–11406.64	90	11326.35	0.3650	0.0192
11629.96–11777.67	122	11707.37	0.3913	0.0175
11987.99–12121.68	81	12050.25	0.3881	0.0235

Table B.23. HD 158614 S-index observing seasons (in JD-2440000).

JD range	N _{obs}	JD _{mean}	S _{mean}	σ_S
3629.80–3704.80	5	3673.40	0.1569	0.0029
3962.80–4051.80	11	4005.89	0.1563	0.0077
4702.98–4875.65	57	4766.81	0.1587	0.0043
5072.99–5212.69	135	5149.34	0.1603	0.0051
5383.05–5590.69	240	5506.64	0.1581	0.0037
5736.06–5981.65	351	5859.77	0.1580	0.0050
6162.01–6329.64	18	6264.95	0.1577	0.0027
6548.96–6695.63	30	6622.91	0.1572	0.0035
6919.99–7056.69	54	6981.74	0.1570	0.0044
7254.01–7422.67	33	7334.77	0.1589	0.0039
7654.96–7759.70	14	7714.52	0.1598	0.0027
8074.78–8135.66	12	8106.23	0.1613	0.0029
8360.01–8493.67	180	8428.77	0.1630	0.0033
8695.01–8871.68	59	8785.47	0.1616	0.0027
9131.94–9252.64	27	9190.68	0.1616	0.0038
9493.93–9610.64	33	9551.79	0.1579	0.0034
9887.83–9986.63	18	9944.40	0.1572	0.0036
10222.91–10311.71	24	10262.94	0.1555	0.0038
10527.02–10703.66	36	10616.00	0.1557	0.0040
10925.86–11065.66	24	11008.03	0.1568	0.0054
11283.98–11421.66	27	11353.70	0.1562	0.0060
11647.99–11793.66	34	11718.38	0.1560	0.0035
12012.96–12138.68	27	12076.93	0.1608	0.0055

Table B.24. HD 161239 S-index observing seasons (in JD-2440000).

JD range	N _{obs}	JD _{mean}	S _{mean}	σ_S
4423.72–4525.65	167	4468.22	0.1379	0.0036
4674.02–4900.62	164	4803.73	0.1333	0.0043
5073.02–5235.67	177	5143.14	0.1319	0.0042
5367.11–5621.62	212	5516.38	0.1374	0.0049
5758.05–5996.62	194	5914.49	0.1432	0.0065
6204.00–6342.64	105	6283.13	0.1370	0.0045
6548.99–6693.67	125	6619.66	0.1339	0.0041
6948.97–7079.62	90	7017.39	0.1319	0.0044
7295.98–7433.64	108	7358.13	0.1351	0.0046
7663.92–7804.61	61	7733.26	0.1423	0.0044
8070.82–8153.65	42	8112.66	0.1388	0.0040
8395.95–8499.67	36	8456.55	0.1338	0.0029
8732.94–8902.65	108	8835.91	0.1332	0.0033
9153.89–9254.66	75	9208.25	0.1364	0.0049
9476.97–9619.64	126	9556.65	0.1381	0.0041
9873.91–9986.67	54	9944.52	0.1360	0.0034
10222.94–10362.62	96	10295.11	0.1335	0.0047
10534.99–10726.62	120	10640.45	0.1320	0.0040
10953.95–11074.63	69	11014.57	0.1316	0.0040
11287.97–11429.66	48	11359.94	0.1385	0.0052
11657.98–11794.66	76	11725.45	0.1376	0.0047
12017.97–12152.64	60	12098.48	0.1305	0.0048

Table B.25. HD 182572 S-index observing seasons (in JD-2440000).

JD range	N _{obs}	JD _{mean}	S _{mean}	σ_S
4733.99–4900.67	39	4811.69	0.1536	0.0071
5120.93–5261.67	153	5190.78	0.1469	0.0046
5441.01–5595.68	206	5525.31	0.1507	0.0048
5805.02–6016.63	230	5887.47	0.1487	0.0060
6223.97–6357.62	102	6296.96	0.1462	0.0033
6577.96–6721.65	87	6650.17	0.1455	0.0038
6967.98–7107.63	81	7040.55	0.1463	0.0052
7314.93–7465.64	96	7384.17	0.1484	0.0039
7664.97–7809.63	51	7751.02	0.1498	0.0040
8068.90–8178.65	48	8127.01	0.1482	0.0028
8422.91–8499.73	36	8471.48	0.1564	0.0032
8757.93–8918.65	108	8854.01	0.1584	0.0064
9172.89–9296.62	96	9231.99	0.1524	0.0052
9514.95–9670.60	133	9580.67	0.1471	0.0051
9882.91–10018.60	102	9963.26	0.1544	0.0074
10231.97–10385.59	105	10321.17	0.1445	0.0143
10622.90–10727.69	93	10675.26	0.1469	0.0046
10983.92–11120.61	81	11053.91	0.1483	0.0049
11340.98–11487.59	75	11395.28	0.1482	0.0050
11691.94–11837.60	76	11749.68	0.1464	0.0064
12043.98–12182.65	48	12116.24	0.1460	0.0051

Table B.26. HD 185144 S-index observing seasons (in JD-2440000).

JD range	N _{obs}	JD _{mean}	S _{mean}	σ_S
5490.96–5645.68	189	5550.96	0.2414	0.0059
5795.01–6007.65	272	5907.57	0.2357	0.0111
6237.87–6362.62	177	6295.62	0.2161	0.0050
6588.97–6726.62	87	6657.33	0.1928	0.0047
6988.93–7107.63	69	7042.55	0.1863	0.0039
7327.96–7459.61	87	7385.38	0.1865	0.0028
7688.94–7809.64	48	7753.91	0.2113	0.0055
8070.90–8162.65	48	8122.28	0.2384	0.0055
8410.95–8500.76	42	8464.83	0.2206	0.0052
8785.86–8933.64	93	8866.31	0.2212	0.0068
9173.90–9297.61	78	9232.35	0.2012	0.0049
9521.95–9662.62	93	9587.12	0.2082	0.0048
9912.90–10018.61	75	9968.87	0.2366	0.0068
10259.94–10299.79	24	10285.37	0.2295	0.0066

Table B.27. HD 190007 S-index observing seasons (in JD-2440000).

JD range	N _{obs}	JD _{mean}	S _{mean}	σ_S
4423.78–4566.59	238	4481.19	0.7878	0.0596
4742.97–4919.68	291	4833.21	0.6895	0.0437
5109.95–5261.69	204	5181.18	0.7064	0.0618
5476.98–5594.70	75	5530.83	0.8095	0.0615
5838.98–5901.81	48	5872.75	0.7378	0.0566
6024.59–6024.60	3	6024.59	0.7969	0.0238
6238.94–6383.61	108	6310.06	0.7592	0.0411
6610.96–6748.60	79	6676.79	0.7329	0.0369
6989.94–7122.61	99	7060.29	0.6789	0.0869
7347.95–7467.65	106	7406.67	0.6178	0.0459
7688.98–7833.60	53	7759.57	0.6326	0.0508
8068.94–8210.60	84	8130.65	0.6065	0.0318
8420.96–8500.80	57	8468.81	0.6022	0.0355
8785.88–8916.71	108	8860.65	0.5828	0.0397
9204.87–9297.63	78	9246.26	0.5655	0.0585
9521.99–9670.61	123	9580.66	0.6234	0.0421
9908.90–10017.64	42	9982.66	0.6571	0.0368
10283.89–10385.62	75	10333.39	0.6691	0.0659
10636.90–10727.72	69	10682.91	0.6062	0.0554
11022.90–11120.63	48	11065.75	0.6107	0.0272
11357.91–11442.71	31	11399.53	0.5337	0.0290
11720.92–11803.71	33	11763.82	0.5387	0.0172
12082.91–12170.68	27	12133.67	0.6521	0.0418

Table B.28. HD 201091 S-index observing seasons (in JD-2440000).

JD range	N _{obs}	JD _{mean}	S _{mean}	σ_S
3235.80–3415.80	13	3333.65	0.5685	0.0179
3706.80–3805.80	8	3760.80	0.6176	0.0241
3997.80–4170.80	7	4060.66	0.6592	0.0298
4411.84–4566.61	362	4470.91	0.7074	0.0336
4771.92–4900.68	198	4827.73	0.6362	0.0292
5108.94–5274.62	261	5179.45	0.6369	0.0266
5477.96–5668.61	158	5557.99	0.6354	0.0380
5839.97–6041.63	318	5936.69	0.5483	0.0298
6237.90–6406.59	177	6326.08	0.5343	0.0196
6608.95–6759.64	155	6688.55	0.6213	0.0353
6985.97–7140.60	171	7060.96	0.6863	0.0600
7309.97–7482.60	175	7397.03	0.6891	0.0498
7638.95–7850.60	99	7775.10	0.6874	0.0255
8070.94–8220.59	108	8138.61	0.6104	0.0325
8450.95–8551.63	57	8480.61	0.5968	0.0168
8805.93–8973.58	171	8889.45	0.6099	0.0260
9204.92–9300.59	105	9252.81	0.7205	0.0346
9538.95–9671.61	135	9615.18	0.7276	0.0415
9916.95–10038.61	135	9980.84	0.7395	0.0367
10282.95–10421.58	134	10340.02	0.6942	0.0579
10644.87–10776.59	93	10697.45	0.5594	0.0246
11014.92–11150.58	99	11082.68	0.5602	0.0297
11375.88–11509.58	78	11430.25	0.5871	0.0427
11734.90–11867.57	53	11800.79	0.6557	0.0227
12081.95–12182.69	69	12136.20	0.6384	0.0434

Table B.30. HD 206860 S-index observing seasons (in JD-2440000).

JD range	N _{obs}	JD _{mean}	S _{mean}	σ_S
3296.80–3415.80	9	3360.13	0.3157	0.0126
3664.80–3807.80	7	3749.37	0.3291	0.0214
4004.80–4201.80	10	4130.10	0.3350	0.0072
4423.83–4566.64	237	4485.31	0.3249	0.0094
4775.98–4920.66	261	4851.23	0.3207	0.0110
5111.96–5277.64	264	5194.03	0.3182	0.0121
5477.97–5673.67	111	5572.61	0.3358	0.0107
5843.99–6033.65	255	5934.78	0.3283	0.0144
6239.94–6420.60	235	6323.16	0.3312	0.0138
6609.99–6779.58	174	6703.34	0.3436	0.0127
7001.93–7141.62	206	7071.70	0.3213	0.0135
7309.98–7486.59	195	7400.79	0.3079	0.0110
7732.93–7849.60	93	7794.64	0.3345	0.0093
8070.96–8244.58	111	8157.95	0.3323	0.0070
8451.96–8617.65	45	8491.41	0.3285	0.0069
8757.95–8980.60	297	8876.83	0.3336	0.0097
9217.91–9300.62	105	9257.67	0.3206	0.0078
9550.94–9707.58	264	9627.69	0.3385	0.0122

Table B.29. HD 201092 S-index observing seasons (in JD-2440000).

JD range	N _{obs}	JD _{mean}	S _{mean}	σ_S
4411.85–4566.62	386	4473.40	1.1079	0.0822
4771.93–4900.68	195	4828.41	0.9527	0.0793
5108.94–5274.62	261	5179.45	0.9435	0.0453
5477.97–5668.62	162	5558.27	0.9547	0.0553
5839.97–6041.62	318	5936.69	0.9539	0.0559
6237.90–6406.60	180	6325.78	0.9757	0.0789
6608.96–6759.65	156	6688.46	0.9537	0.0510
6985.98–7140.60	156	7066.39	0.9407	0.0630
7309.97–7482.61	178	7397.30	0.9678	0.0852
7638.96–7850.61	99	7775.11	1.0511	0.0860
8070.95–8220.60	107	8138.47	1.0371	0.0435
8450.96–8551.64	57	8480.62	0.9338	0.0399
8805.93–8973.59	170	8888.97	0.9538	0.0554
9204.93–9300.59	120	9248.88	0.9391	0.0497
9538.96–9671.61	129	9613.72	0.8614	0.0505
9916.95–10038.61	135	9980.84	0.9393	0.0490
10282.95–10421.59	129	10340.50	0.7981	0.0502
10644.86–10776.58	92	10697.49	0.7747	0.0333
11014.91–11150.59	95	11082.52	0.9436	0.0784
11375.88–11509.58	84	11435.61	1.0877	0.0615
11734.90–11867.57	60	11801.70	0.9965	0.0966
12081.95–12182.68	69	12136.20	0.9553	0.0881

HD	$B - V$	$\log R'_{\text{HK}}$	P_{rot} (days)	P_{cyc} (yr)	$P_{\text{cyc,phot}}^{\text{long}}$ (yr)	$P_{\text{cyc,chrom}}$ (yr)	amp_{phot} (*10 ⁻³ mag)	$\text{amp}_{\text{chrom}}$ (*10 ⁻³)	$\Delta\phi$	flag _{phot}	flag _{chrom}	χ^2_{phot}	χ^2_{chrom}	χ^2_{sim}
1835	0.66	-4.445	7.76	7.07 ± 0.02	-	28.1	6.56 ± 0.45	11.90 ± 0.15	0.62 ± 0.01	2	2	0.72	3.71	3.06
10476	0.84	-4.938	35.00	10.33 ± 0.02	-	-	1.23 ± 0.07	13.98 ± 0.08	-0.04 ± 0.01	2	3	1.01	9.82	7.27
13421	0.56	-5.217	17.00	7.71 ± 0.05	-	-	0.66 ± 0.04	1.20 ± 0.04	0.17 ± 0.01	1	1	4.26	2.12	2.48
18256	0.43	-4.758	3.00	7.65 ± 0.02	-	-	0.96 ± 0.08	7.39 ± 0.07	0.04 ± 0.01	1	1	1-2	1.31	10.44
20630	0.68	-4.420	9.21	6.03 ± 0.01	-	-	14.12 ± 0.50	14.50 ± 0.12	0.54 ± 0.01	3	2-3	0.35	6.09	5.17
25998	0.46	-4.489	2.00	4.51 ± 0.01	-	65.5	2.84 ± 0.29	4.54 ± 0.11	0.55 ± 0.01	3	2	0.97	4.12	3.80
35296	0.53	-4.438	4.00	4.16 ± 0.01	-	26.9	1.87 ± 0.32	4.54 ± 0.06	0.51 ± 0.03	3	1-2	0.30	6.60	5.76
39587	0.59	-4.460	5.00	6.24 ± 0.01	-	16.7	2.52 ± 0.47	5.28 ± 0.05	0.54 ± 0.03	2	1-2	0.55	9.02	8.27
72905	0.62	-4.375	4.91	4.22 ± 0.03	-	-	4.25 ± 0.33	6.94 ± 0.24	0.71 ± 0.02	2-3	2	0.62	2.46	1.48
75332	0.49	-4.474	4.00	10.91 ± 0.13	-	721.7	5.41 ± 0.29	2.65 ± 0.12	0.48 ± 0.01	1	1	0.35	5.02	3.82
81809	0.64	-4.927	41.00	8.19 ± 0.01	-	-	0.63 ± 0.06	10.07 ± 0.08	0.08 ± 0.01	1	3	2.65	2.79	2.75
82443	0.77	-4.211	5.42	2.69 ± 0.01	-	11.3	6.49 ± 0.27	35.83 ± 0.46	0.57 ± 0.01	3	2	0.70	3.90	2.52
82885	0.77	-4.674	18.00	9.29 ± 0.01	-	30.5	2.42 ± 0.21	15.93 ± 0.12	0.40 ± 0.01	1	1	1-2	0.61	11.20
103095	0.75	-4.899	31.00	7.20 ± 0.01	-	-	0.69 ± 0.05	12.68 ± 0.11	-0.10 ± 0.01	1	3	1.35	2.38	2.15
115383	0.59	-4.486	3.00	6.51 ± 0.03	-	29.4	4.15 ± 0.23	3.32 ± 0.13	0.34 ± 0.01	2	2-3	0.49	6.77	4.20
115404	0.94	-4.529	18.00	10.31 ± 0.03	70.2	-	2.37 ± 0.33	32.09 ± 0.27	0.34 ± 0.02	2	1-2	0.13	5.83	4.08
120136	0.48	-4.742	4.00	5.60 ± 0.01	15.9	-	1.30 ± 0.13	2.46 ± 0.03	0.03 ± 0.02	1-2	1-2	0.29	4.77	3.74
124570	0.54	-5.156	26.00	-	-	-	-	-	-	-	-	-	-	-
129333	0.61	-4.148	2.68	10.22 ± 0.38	547.0	15.9	14.89 ± 1.78	1.33 ± 0.49	0.33 ± 0.05	3	2	0.15	1.76	1.11
131156A	0.76	-4.387	6.00	3.54 ± 0.00	-	-	6.87 ± 0.70	16.93 ± 0.08	0.53 ± 0.02	1-2	1	0.47	40.04	36.67
143761	0.60	-5.046	17.00	-	-	-	-	-	-	-	-	-	-	-
149661	0.82	-4.613	21.00	11.60 ± 0.02	40.2	-	3.26 ± 0.36	26.83 ± 0.11	0.47 ± 0.02	1-2	2	0.54	16.15	13.82
158614	0.72	-5.023	34.00	11.00 ± 0.10	253.6	-	1.07 ± 0.15	2.74 ± 0.10	0.23 ± 0.02	2	3	1.08	2.16	1.99
161239	0.65	-5.180	29.00	5.03 ± 0.01	-	-	1.33 ± 0.11	4.23 ± 0.06	-0.04 ± 0.01	2	3	2.30	2.53	2.51
182572	0.77	-5.093	41.00	12.51 ± 0.07	-	-	0.86 ± 0.05	3.35 ± 0.07	0.17 ± 0.01	2-3	3	1.97	8.51	6.73
185144	0.79	-4.823	27.00	6.55 ± 0.01	19.1	-	0.63 ± 0.11	21.43 ± 0.09	-0.06 ± 0.03	1	3	0.80	21.44	15.58
190007	1.14	-4.711	29.00	8.98 ± 0.03	-	38.0	4.36 ± 0.28	39.17 ± 0.53	0.48 ± 0.01	3	2	0.60	6.05	4.61
201091	1.18	-4.765	35.00	7.13 ± 0.00	-	-	0.58 ± 0.13	72.88 ± 0.18	0.00 ± 0.04	2-3	3	0.78	20.92	17.78
201092	1.37	-4.910	38.00	-	-	-	-	-	-	-	-	-	-	-
206860	0.59	-4.416	4.84	5.36 ± 0.02	-	-	4.44 ± 0.49	6.37 ± 0.11	0.41 ± 0.02	2	2	0.46	5.18	4.66

Table 2. Physical parameters of the sample. $B - V$ colors and activity levels $\log R'_{\text{HK}}$ have been adopted from Lockwood et al. (2007) and Baltunas et al. (1996). Rotation periods have been taken from Baltunas et al. (1996) and Messina & Guinan (2002). Cycle periods P_{cyc} are the best sine fit periods to both data sets simultaneously. Possible long periods subtracted from the photometric and chromospheric time series are given by $P_{\text{cyc,phot}}^{\text{long}}$ and $P_{\text{cyc,chrom}}^{\text{long}}$, respectively. The amplitudes to the photometric and the chromospheric time series are given by amp_{phot} and $\text{amp}_{\text{chrom}}$, respectively. The phase difference between the two time series is indicated with $\Delta\phi$. The values for flag_{phot} and flag_{chrom} provide quality flags for the goodness of the periodicity in the respective time series. The values are in place of 1 = weak periodicity, 2 = moderate to good periodicity, 3 = excellent periodicity. The last three columns contain the reduced chi-square values of the fit to the photometric, chromospheric, and combined time series, respectively.